Journal of Volcanology and Geothermal Research 362 (2018) 32–48

Contents lists available at ScienceDirect

Journal of Volcanology and Geothermal Research

journal homepage: www.elsevier.com/locate/jvolgeores

The impact of particle shape on fall velocity: Implications for volcanic ash dispersion modelling

Jennifer Saxby [a,*], Frances Beckett [b], Katharine Cashman [a], Alison Rust [a], Eleanor Tennant [a]

[a] Dept. Earth Sciences, University of Bristol, Queen's Road, Bristol BS8 1RJ, UK
[b] Met Office, FitzRoy Road, Exeter EX1 3PB, UK

ARTICLE INFO

Article history:
Received 23 April 2018
Received in revised form 16 August 2018
Accepted 20 August 2018
Available online 23 August 2018

ABSTRACT

Modelling atmospheric volcanic ash dispersion is a critical tool in mitigating the impact of large explosive eruptions; it is also useful for understanding and reconstructing past events. Most atmospheric dispersion models include a sedimentation velocity term that is sensitive to the physical properties of the particle, but many do not use particle shape as an input parameter; instead particles are assumed to be spherical. There are many empirical and semi-empirical shape-dependent drag laws. We measure the velocity of scaled analogue particles over the range of flow conditions anticipated for volcanic ash dispersion to test published formulae against an independent dataset. We use a semi-empirical formula we determined to be accurate for non-spheres to investigate the sensitivity of the modelled transport of an ash cloud to particle shape, using the atmospheric dispersion model NAME and a shape parameter we measure for non-spherical ash particles from Katla volcano, Iceland. We find that model particle trajectories are sensitive to particle shape for particles >1–3 μm diameter; the sedimentation velocity of smaller particles is low compared to atmospheric vertical velocities. Sensitivity to shape increases with size such that 100 μm particles can travel 44% further from the source when they are highly non-spherical (sphericity = 0.5). Despite the sensitivity of the fall velocity of large particles to their shape, however, forecasts of distal ash concentration using particle size distributions of 0.1–100 μm and 0.1–250 μm show relatively good agreement between a spherical and non-spherical case for the first 36 h after an eruption. The vertical structure of an ash cloud is more sensitive to particle shape than the horizontal extent. Model particle trajectories are also sensitive to particle size, and we find a discrepancy between different particle size parameters for non-spherical ash: particle long axis L, used in cryptotephra studies, was on average twice the equivalent-volume sphere diameter d_v, used in dispersion modelling, for tephra samples from Katla volcano, Iceland. This discrepancy in size measurements could explain the observed travel distance of large distal cryptotephra shards.

1. Introduction

The ability to forecast the atmospheric transport of volcanic ash is crucial for mitigating the potential impact to aircraft, respiratory health, agriculture, and infrastructure (Stevenson et al., 2013; Giehl et al., 2016). Dispersion modelling can also aid in reconstructing past events: cryptotephra layers, distal and widespread volcanic ash deposits from large explosive eruptions, can be linked to their source volcano to provide an age framework for the host sediment (e.g. Wastegård, 2002). Dispersion modelling has the potential to constrain ash source regions for these eruptions. Modelling can also provide insights into the dynamics of past large eruptions in the absence of modern analogues, for example the ~39 ka Campanian Ignimbrite (Italy; Costa et al., 2012), the ~74 ka Younger Toba Tuff (Indonesia) and the ~340 ka Whakamaru eruption of Taupo (New Zealand; Matthews et al., 2012).

To model the dispersion of an ash cloud the sedimentation of the particles must be represented. The fall velocity of a particle is governed by its physical properties, including its shape; for a given volume and density, non-spherical particles fall more slowly than spheres (e.g. Haider and Levenspiel, 1989). Eruptive processes produce a wide range of volcanic ash morphologies, making an accurate description of particle shape challenging (Liu et al., 2015). In addition, there are multiple empirical and semi-empirical correlations between shape and fall velocity for volcanic particles or analogues (Wilson and Huang, 1979; Haider and Levenspiel, 1989; Ganser, 1993; Dellino et al., 2005; Bagheri and Bonadonna, 2016; Dioguardi et al., 2017, 2018), but little published literature compares the formulae or assesses their use in atmospheric dispersion models. An assessment of shape formulae for modelling particle travel distance is necessary because there is a recognised discrepancy in distal grain size data between the fields of

* Corresponding author at: School of Earth Sciences, University of Bristol, Wills Memorial Building, Queens Road, Bristol BS8 1RJ, UK.
E-mail addresses: jennifer.saxby@bristol.ac.uk (J. Saxby), frances.beckett@metoffice.gov.uk (F. Beckett), kathy.cashman@bristol.ac.uk (K. Cashman), alison.rust@bristol.ac.uk (A. Rust), et16080.2016@my.bristol.ac.uk (E. Tennant).

https://doi.org/10.1016/j.jvolgeores.2018.08.006
0377-0273/

volcanology (deposit sampling), dispersion modelling and satellite ash retrieval (Stevenson et al., 2015). Moreover, dispersion modelling has been unable to account for the observed travel distances of large, typically >80 μm, volcanic ash shards in cryptotephra deposits (Beckett et al., 2015; Stevenson et al., 2015; Watson et al., 2016). We hypothesise that particle shape may control tephra dispersion as very distal cryptotephra deposits from large explosive eruptions often contain abundant flat, platy shards (Mangerud et al., 1984; Blockley et al., 2007; Stevenson et al., 2015; Cashman and Rust, 2016).

We measure the velocity of scaled analogue particles to evaluate empirical shape formulae. In doing so we compare empirical schemes for estimating fall velocity using an independent dataset and use this to determine the most appropriate scheme for modelling the dispersion of non-spherical ash. We then measure the shape of ash particles from Katla volcano, Iceland, using 2D and 3D measurement techniques to compare the resulting shape data; we then use the data to investigate the sensitivity of the atmospheric dispersion model NAME (Numerical Atmospheric-dispersion Modelling Environment; Jones et al., 2007) to the formula we determine to be most accurate for non-spheres (Ganser, 1993), compared to an analytical solution for spheres (White, 1974). We assess both the sensitivity of maximum particle travel distance, important for understanding the distribution of cryptotephra particles (Stevenson et al., 2015), and distal atmospheric ash concentrations, with implications for ash forecasting. In this way we bring together the disciplines of physical volcanology and dispersion modelling to gain a greater understanding of the benefits and limitations of measuring particle shape and its uses as a dispersion model input parameter.

2. Background

Atmospheric dispersion models are numerical solutions describing physical and chemical processes within a suspended plume in response to atmospheric conditions (Holmes and Morawska, 2006). Models include a source term, which describes the location and magnitude of the source; source terms range from complex plume dynamics models to simple point sources. The particles are then dispersed according to meteorological (met) data from an atmospheric model, and processes such as sedimentation and deposition, which are controlled by a transport model. Eulerian transport models solve for particle concentration over a fixed computational grid (e.g. FALL3D; Costa et al., 2006), whereas Lagrangian transport models calculate trajectories of model particles representing the mass of many real particles (e.g. HYSPLIT; Draxler and Hess, 1997). Both model types solve advection-diffusion equations, in which chemical or particulate pollutants are released from a source and dispersed passively (i.e. do not alter the flow conditions) according to wind velocity (advection) and atmospheric turbulence (diffusion). Heavy particulates, including volcanic ash, are also subject to sedimentation (gravitational settling).

In the Lagrangian model NAME (Jones et al., 2007), the behaviour of particulates in the vertical is determined by vertical velocity w:

$$w = w_a - w_{sed} + w', \tag{1}$$

where w_a is wind advection, w′ is turbulent diffusion, and w_{sed} is sedimentation velocity. We can assume w_{sed} is equal to particle terminal velocity w_t, the velocity a particle obtains when its weight is balanced by air resistance such that the net force acting on the particle is zero and it no longer accelerates; fine particles reach terminal velocity in the atmosphere over distances that are negligible compared to plume height. Terminal velocity is a function of physical particle properties including size, density and shape, as well as atmospheric density and viscosity, which vary with altitude (Jones et al., 2015). Particle removal processes can include impact on the ground surface (dry deposition; Webster and Thomson, 2011) and removal by precipitation (wet deposition; Webster and Thomson, 2014).

2.1. Modelling sedimentation

Scaling requires that terminal velocity be defined as a function of the dimensionless drag coefficient C_D. Terminal velocity w_t is calculated by:

$$w_t = \left(\frac{4}{3}\frac{d}{C_D} g \frac{\rho_P - \rho}{\rho}\right)^{\frac{1}{2}}, \tag{2}$$

where d is a characteristic particle dimension, g is gravitational acceleration (9.81 m s^{-1}), ρ is fluid density, and ρ_P is particle density. Parameters with a first order impact on C_D are shape and orientation (Bagheri and Bonadonna, 2016), particle/fluid density ratio, and Reynolds number (Re), the ratio of inertial to viscous forces:

$$Re = \frac{\rho w_T d}{\mu}, \tag{3}$$

where μ is the dynamic viscosity of the fluid. When Re is <0.1 such that there is no wake at the rear of a falling particle (Stokes flow), C_D for rigid spherical particles is well approximated by Stokes' Law:

$$C_D = \frac{24}{Re} \tag{4}$$

(Clift et al., 2005). At higher Re, the flow passes into a transitional state known as the intermediate regime. Between Re = 20 and Re = 130, an attached wake forms and increases in size downstream of the particle. From Re ≈ 1000, the flow around a particle is fully turbulent (Clift and Gauvin, 1971). In this turbulent regime, C_D does not significantly change with Re; it can be considered a function of particle shape alone (Chhabra et al., 1999).

Irregular particles can have high surface curvature, a relatively large surface area over which to develop friction, and a tendency to display secondary oscillations during settling. All these factors mean that C_D of a highly irregular particle can be up to many orders of magnitude higher than that of a sphere (Dietrich, 1982). Variability in magma properties and fragmentation mechanisms means that ash particles can have rough surfaces and low density (micropumice) or be extremely non-spherical (glass shards), making their terminal velocity difficult to anticipate (Dellino et al., 2005; Loth, 2008).

Analytical drag laws allow accurate velocity calculation for spheres (e.g. Clift and Gauvin, 1971; White, 1974) and a limited range of ellipsoidal shapes (e.g. Bagheri and Bonadonna, 2016) over a wide Re range. Analytical solutions do not exist for flow around irregular particles; instead, empirical correlations are used. For meaningful comparison between particles, it is necessary to have a consistent definition for particle dimension d, although even with this condition C_D is sensitive to particle shape (Wilson and Huang, 1979). Since the drag coefficient of spheres can be determined analytically, most empirical sedimentation schemes define d as d_v, the diameter of a volume-equivalent sphere; C_D is then a function of one or more geometric ratios which compare the particle being described to a sphere (Clift et al., 2005). An example is sphericity ψ, the ratio of the surface area of a volume-equivalent sphere to the surface area of the particle (Wadell, 1933); a ψ of 1 indicates perfect sphericity and a ψ close to 0 indicates extreme non-sphericity. Particles with different shapes can have the same sphericity; this caveat is unavoidable if a small number of easily measurable shape descriptors are needed to describe an infinite number of possible morphologies (Clift et al., 2005). Another class of particle descriptors, termed form factors, use ratios between principal axis lengths (Wilson and Huang, 1979; Bagheri and Bonadonna, 2016); these have the advantage of being simpler to measure than surface area for irregular particles, and they are less sensitive to image resolution (Liu et al., 2015). However, form factors do not describe small-scale surface roughness, which increases C_D (Achenbach, 1974). The most meaningful shape descriptor for any application is therefore dependent on the

morphological variability of the particles. An important caveat of empirical correlations is that they are only valid within the Re range of the experiments on which the correlation is based.

2.2. Volcanic ash forecasting

Monitoring and operational forecasting of volcanic ash clouds is carried out worldwide by nine Volcanic Ash Advisory Centres (VAACs; ICAO, 2012), each responsible for a discrete region of airspace. VAACs use atmospheric dispersion models to forecast ash transport in the atmosphere following an eruption. The eruptive source can be characterised by its location, dimensions, vertical distribution of ash, plume phases (e.g. gas, particulates), and mass eruption rate (Hort, 2016). Most VAACs model volcanic ash as sedimenting particles, with the exception of the Montreal VAAC, which by default treats ash as a non-sedimenting particle (D'Amours et al., 2010). The remaining VAACs calculate particle terminal velocity as a function of physical particle properties, including size (as a single value or particle size distribution), density, and shape. The Buenos Aires, Tokyo and Darwin VAACs operationally model non-sphericity (Hort, 2016). For example, the Buenos Aires VAAC uses the Fall3D dispersion model (Folch et al., 2009), which calculates sedimentation velocity using the Ganser (1993) sedimentation scheme with a default sphericity of 0.9 (Reckziegel et al., 2016), and the option to vary sphericity for each particle class if shape data are available.

In this study we focus on the operational setup of the London VAAC, which uses the NAME dispersion model. NAME is maintained and developed by the Met Office, UK, and has been used operationally to provide forecasts of pollutant dispersion for a wide range of applications, including for crises such as the 2005 Buncefield oil depot explosion (Webster et al., 2007) and the Fukushima power plant accident in 2011 (Leadbetter et al., 2015), as well as daily resuspended ash forecasts for southern Iceland (Liu et al., 2014; Beckett et al., 2017) and routine air quality forecasts for the UK (Jones, 2004). The London VAAC is responsible for providing forecasts of volcanic ash clouds for the domain covering Iceland, Scandinavia, the UK, and the north-eastern part of the north Atlantic. Most recently they provided forecasts for ash clouds from the eruptions of Eyjafjallajökull in 2010 and Grimsvötn in 2011 (Webster et al., 2012). For London VAAC forecasts (and by default where no scheme is specified), NAME calculates particle terminal velocity using the White (1974) analytical formula for spheres.

The main applications of volcanic ash forecasting are to prevent aircraft encounters with high concentrations of volcanic ash during or shortly after an eruption (Folch, 2012). The VAACs produce Volcanic Ash Graphics (VAGs) and accompanying text documents, Volcanic Ash Advisories (VAAs), which depict the forecast location of the ash cloud out to T + 18 h. However, also important is the long-term transport of ash particles and sulfate aerosols in the stratosphere, which can cause climate forcing by affecting the atmospheric radiative budget over months or years (e.g. Lacis et al., 1992). Direct sampling of the El Chichón ash cloud, for example, has indicated that particles >5 μm can remain in the stratosphere for at least 6 months (Gooding et al., 1983); this may be due to slow settling of irregular shapes and low-density aggregates (Gooding et al., 1983; MacKinnon et al., 1984). Our conclusions on particle behaviour using NAME, however, are time-dependent and specific to the problem of forecasting volcanic ash concentration in the hours to days after an eruption.

In the absence of measurements of physical particle properties during an eruption, the London VAAC uses a default particle size distribution (PSD) based on grain size distributions from eruptions of Mount *St* Helens, Augustine, and Redoubt volcanoes (Hobbs et al., 1991), and assumes a density of 2300 kg m^{-3} (suitable for rhyolite glass). The setup considers particles from 0.1–100 μm, with larger particles assumed to fall out close to the volcano (Witham et al., 2017). Importantly, the model sedimentation equations use volume-equivalent sphere diameter (d_v), while the Hobbs et al. (1991) PSD is determined from forward light scattering measurements by airborne instruments. The scattering properties of particles are dependent on particle shape, and therefore diameters determined by scattering coefficients are unlikely to be equal to d_v. Alternatively, PSDs from ground-based sampling studies are often determined by sieving the volcanic ash samples; although sieve size is also unlikely to be equivalent to d_v, especially for particles with very irregular shapes (Garboczi et al., 2017).

Beckett et al. (2015) found that NAME volcanic ash forecasts are sensitive to PSD, with density and shape having lesser but still signifcant impacts. They show, for example, that a $d_v = 100$ μm particle of $\psi_R = 0.4$ could travel up to 60% further than a spherical particle of equivalent volume. Here the shape descriptor ψ_R is a 2D measure of sphericity based on particle projected area and perimeter (Riley et al., 2003). 2D shape descriptors are often used as substitutes for 3D sphericity ψ due to the difficulty in obtaining surface area and volume measurements of fine ash particles. However, the sensitivity of the Ganser (1993) scheme to the method of sphericity measurement has not been evaluated.

2.3. Quantifying ash morphology

To assess the discrepancy between ψ and ψ_R, and to provide a shape parameter for sensitivity analysis using NAME, we need to quantify the shape of volcanic ash; our samples are chosen for their unusual particle morphology and potential hazard impact. The main source of volcanic ash hazard to the UK and northern Europe is Iceland, with 124 explosive (>95% of magma erupted as tephra) eruptions since written records began around 870 CE (Thordarson and Larsen, 2007). Wind can transport ash from a short explosive eruption in Iceland to any country in Europe within 24 h, with most countries above 50°N subject to a >20% probability of airborne ash concentrations exceeding a 'safe' threshold (Leadbetter and Hort, 2011). Indeed, most cryptotephra layers in northern Europe have been identified by geochemical analysis to originate from Iceland (Lawson et al., 2012). Katla is an active subglacial volcano in Iceland's Eastern Volcanic Zone that is characterised in the Holocene by explosive basaltic eruptions, with over 300 in the last 8400 years (Óladóttir et al., 2005). The average repose interval from 1500 CE to present is 47 years (Larsen, 2000). Less common are eruptions of more evolved Katla (SILK) tephras; these take place with average repose intervals of 100–1000 years, although it is 1700 ^{14}C years since the last known SILK eruption (Larsen et al., 2001). We examine two samples of Katla tephra:

- The Vedde ash is found across northern Europe as a cryptotephra deposit and is thought to originate from an eruption of Katla around 12 ka BP (Wastegård et al., 1998; Lane et al., 2012). The Vedde has a bimodal composition consisting of both basaltic and rhyolitic ash, with SiO_2 contents of 45–58 and 72–76% respectively (Mangerud et al., 1984). It contains characteristic flat, platy rhyolitic glass shards that we interpret as bubble wall fragments (Fig. 1).
- The SILK-LN ash is an intermediate composition (~65% SiO_2) tephra dated to ~ 3.4 ka BP (Larsen et al., 2001; Óladóttir et al., 2005). It contains grains of variable morphology including distinctive 'needles' (Fig. 1), which contain elongate bubbles in a glassy, sparsely crystalline matrix. The SILK-LN tephra forms a widespread deposit in southern Iceland. Its volume on land of 0.12 km^3 DRE (Larsen et al., 2001) suggests an eruption of at least VEI 4 (Newhall and Self, 1982).

3. Evaluation of sedimentation schemes and shape descriptors for non-spherical particles

Particle settling experiments with scaled analogue particles allowed us to systematically vary particle size, shape and density. We used analogue particles with ψ of 0.45 to 0.8 to represent end-member ash geometries (Fig. 1). Geometries were simplified to allow accurate

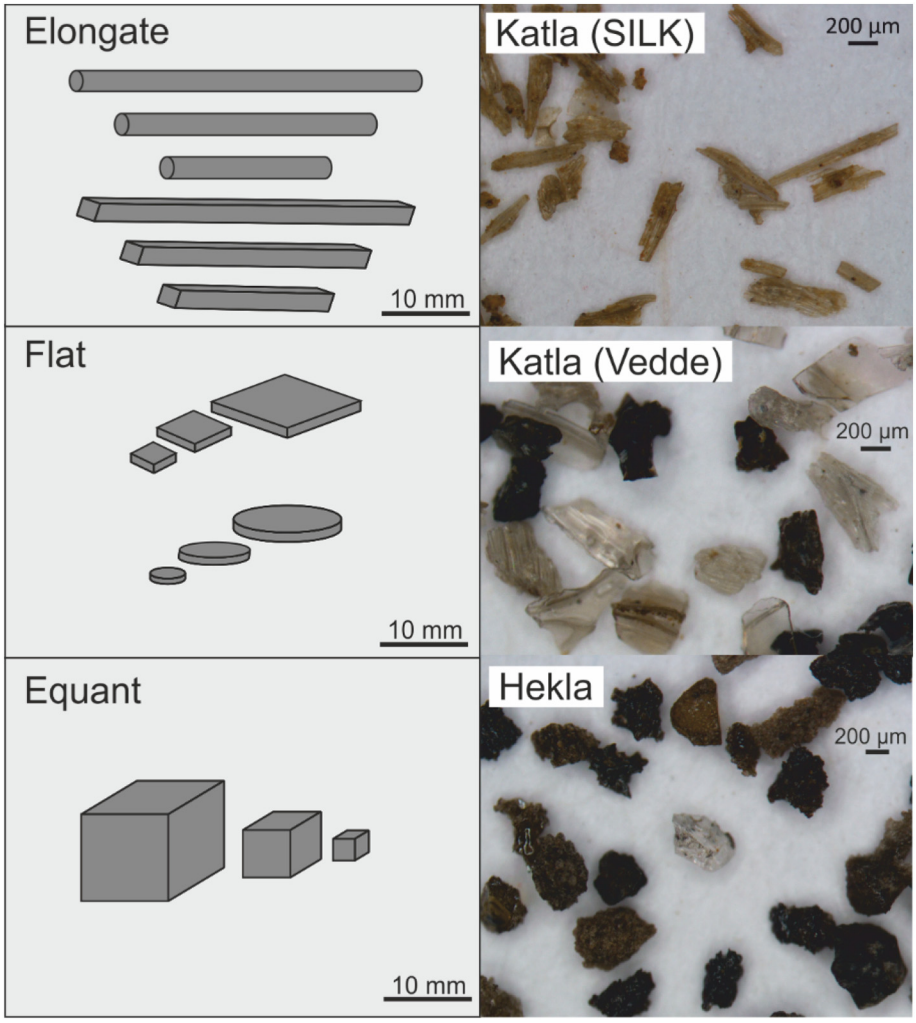

Fig. 1. Particles used in scaled analogue experiments (left), and corresponding example ash morphologies from Katla and Hekla volcanoes, Iceland (right). SILK indicates the SILK-LN tephra layer (~3.4 ka BP; Larsen et al., 2001); the Vedde ash has been dated to 12 ka BP (Wastegård et al., 1998); the Hekla sample is from the 1947 eruption.

particle characterisation and measurement of multiple complex shape descriptors. Particle and fluid properties (Table 1) were adjusted to create flow conditions relevant to volcanic ash dispersion. The Re range of the experiments ($7.6 \times 10^{-7} < Re < 2316$) is characteristic of volcanic ash of about 0.6–2800 μm diameter falling in air (assuming spherical particles, a density of 2300 kg m^{-3}, atmospheric density of 1.225 kg m^{-3}, and atmospheric viscosity of 1.98×10^{-5} Pa.s). For comparison, most VAACs operationally model particles ≤ 100 μm (Hort, 2016); however, in large eruptions particles > 100 μm comprise a substantial mass fraction of far-travelled deposits (Cashman and Rust, 2016). Extending our experiments to higher Re (i.e. higher equivalent ash diameter) also allowed us to assess the performance of sedimentation schemes in both Stokes and intermediate flow. As a caveat, we note that the particle-fluid density ratio also has an impact on C_D in the intermediate regime (Bagheri and Bonadonna, 2016), and that the range of experimental particle-fluid density ratios (~1.1–2.1) is much lower than the density ratio expected for ash falling in air (~2000).

We recorded the velocity of analogue particles in a 40 × 40 × 70 cm clear Perspex tank filled with water, glycerine, a 70% volume glycerine-water solution, or glucose syrup. Particle trajectories were filmed using a Vision Research Phantom v9.1 high-speed video camera with a frame rate of 1000 fps. The video data were processed with Phantom Camera Control and ImageJ software. We recorded vertical velocity, but particles also moved laterally. For this reason, we placed a mirror at 45° to the edge of the tank to give an orthogonal view and allow trigonometric calculation of each particle's exact vertical position. Terminal velocity was calculated as the mean of five repeat measurements for each particle-fluid combination; we then calculated Re and C_D as a function of w_t. We ensured each particle reached terminal velocity by measuring velocity as a function of depth and only including data averaged over a

Table 1
Physical properties of particles and fluids used in scaled analogue experiments.

Fluid	Fluid density ρ (at 17.5 °C), kg·m^{-3}	Fluid viscosity μ (at 17.5 °C), Pa·s	Particles	Particle density ρ_P, kg·m^{-3}	Reynolds number (Re) range	Flow regime(s)
Glucose syrup	1419.44	206.9	Aluminium	2707	7.6×10^{-7}–4.0×10^{-5}	Stokes
Glycerine	1262.6	1.7882	PVC	1431	3.3×10^{-4}–0.07	Stokes
			Aluminium	2707	3.3×10^{-3}–0.09	Stokes
70% glycerine 30% water	1194.6	0.040533	PVC	1431	2–56	Intermediate
Water	998.51	0.0010696	PVC	1431	165–2316	Intermediate, turbulent

Table 2
Mathematical description of drag calculations for the sedimentation schemes used in this study.

Sedimentation scheme	C_D definition	Shape descriptor	Experimental Re range
White (1974)	$C_D = C_1 + \frac{24}{Re} + \frac{C_2}{1+\sqrt{Re}}$ where $C_1 = 0.25$ and $C_2 = 6.0$ for $Re < 5 \times 10^3$.	None	–
Ganser (1993)	$C_D = \frac{24}{ReK_S}\,(1 + 0.1118[\,Re(K_S K_N)]^{0.6567}) + \frac{0.4305K_N}{1+\frac{3305}{ReK_S K_N}}$ where K_N is a correction factor for turbulent flow: $K_N = 10^{1.84148(-Log\psi)^{0.5743}}$ and K_S is a correction factor for laminar (Stokes) flow: $K_S = \frac{3}{1+2\psi^{-0.5}}$	Sphericity: $\psi = \frac{\pi^{\frac{1}{3}}(6V_p)^{\frac{2}{3}}}{A_p}$ Riley's sphericity (Riley et al., 2003): $\psi_R = \frac{4\pi A_{proj}}{P_p^{\,2}}$	$Re < 2.5 \times 10^4$
Wilson and Huang (1979)	$C_D = \frac{24}{Re}F^{-0.828} + 2\sqrt{1.07-F}$	Form factor F: $F = (I + S)/2L$	$0.54 < Re < 79.1$
Bagheri and Bonadonna (2016)	$C_D = \frac{24K_S}{Re}\,(1 + 0.125(\,Re\,K_N/K_S)^{2/3}) + \frac{0.46K_N}{1+5330/(\,Re\,K_N/K_S)}$ where: $K_s = (F_s^{\frac{1}{3}} + F_s^{-\frac{1}{3}})/2$ $K_N = 10^{\alpha_2[-\log(F_N)]^{\beta_2}}$ $\alpha_2 = 0.45 + 10/\exp(2.5\log\rho' + 30)$ $\beta_2 = 1 - 37/\exp(3\log\rho' + 100)$ $F_s = f\,e^{1.3}\,(\frac{d_n^3}{LIS})$ $F_N = f^2\,e\,(\frac{d_n^3}{LIS})$	Flatness f: $f = S/I$ Elongation e: $e = I/L$	$Re < 3 \times 10^5$
Dioguardi et al. (2017)	$C_D = \frac{4}{3}\,\frac{0.559C_{D,\ sphere}(\,Re^{4.18\psi^{-\,Re^{-0.2}}})^{0.5134}}{Re^2}$ where $C_{D,\ sphere}$ is calculated after Clift and Gauvin (1971): $C_{D,sphere} = \frac{24}{Re}\,(1 + 0.15\,Re^{0.687}) + \frac{0.42}{1+\frac{42500}{Re^{1.16}}}$	Sphericity: $\psi = \frac{\pi^{\frac{1}{3}}(6V_p)^{\frac{2}{3}}}{A_p}$	$0.03 < Re < 10^4$

depth range with constant velocity. The impact of boundary wall proximity on velocity was corrected using the approach of Chhabra et al. (1996) and Chhabra (1995); see Appendix A for details.

To compare measured w_t to published drag laws, we calculated theoretical w_t and Re using eqs. (2–3), and C_D using an analytical solution for spheres (White, 1974) and empirical solutions using one or more geometric shape descriptors (Wilson and Huang, 1979; Ganser, 1993; Bagheri and Bonadonna, 2016; Dioguardi et al., 2017). These formulae are summarised in Table 2. For empirical correlations, the Re range of experiments is given; however, the schemes of Ganser (1993) and Bagheri and Bonadonna (2016) are semi-empirical schemes that use globally convergent formulae. The resulting nonlinear equation systems were solved using a Matlab code which iterates to convergence, using w_t of an equivalent-volume sphere in Stokes flow as an initial guess.

We calculated geometric shape descriptors (Table 2) using digital caliper measurements. Where it was necessary to use two-dimensional particle measures (e.g. area, perimeter), these were calculated for the particle's maximum projected area, as particles falling stably are often orientated with maximum area in the direction of fall (Christiansen and Barker, 1965; Dietrich, 1982). However, particles falling in the intermediate regime tend to change orientation as they fall (Willmarth et al., 1964; Wilson and Huang, 1979; this study).

We used the parameterisation of Cheng (2008) to calculate density and viscosity of glycerine-water solutions from the volume fraction of glycerine and the temperature. The density and viscosity of glucose syrup were calculated from w_t of a metal sphere dropped in the fluid. Particle densities were calculated from mass and volume measurements and checked using relative weights in air and water and Archimedes' principle of buoyancy.

To validate this procedure, Fig. 2 shows theoretical and observed velocities for 2–10 mm diameter glass and metal spheres, for an Re range of 28–5600 using glycerine solutions of 30–70% by volume. Mean velocities deviate from the analytical solution (White, 1974) by a maximum of 8.2%. This is taken to represent the raw measurement error on the data. Standard errors are small (0.2–2.2%) and in many cases do not intersect with the analytical solution; we therefore assume that the main sources of error are the particle and fluid properties, e.g. ρ_P, rather than velocity measurement. We note that standard error for non-spherical particles in this study is higher (0.2–13.3%) as C_D depends on projected area in the direction of fall (Leith, 1987), such that non-spherical particles show a range of w_t dependent on orientation.

3.1. Particle settling data

Results of settling experiments are shown in Fig. 3 for the Stokes, intermediate and turbulent flow regimes. Velocity data are available in Appendix B. For a given Reynolds number Re, the drag coefficient C_D of a non-spherical particle is higher than for an analytical solution for spheres. The data show overlap with the C_D range in volcanic ash settling experiments by Dioguardi et al. (2017); this suggests that despite geometric differences between the particle shapes used and volcanic ash particles (e.g. the lack of small-scale surface irregularities on analogues) and differences in experimental setup, the drag coefficients obtained here are similar to those of volcanic ash particles. In the upper intermediate flow regime, however, flat and elongate analogue particles have higher C_D than volcanic ash particles of the same Re range (Dioguardi et al., 2017). Dynamic similarity between ash particles and analogues is lower in this regime due to the development of secondary

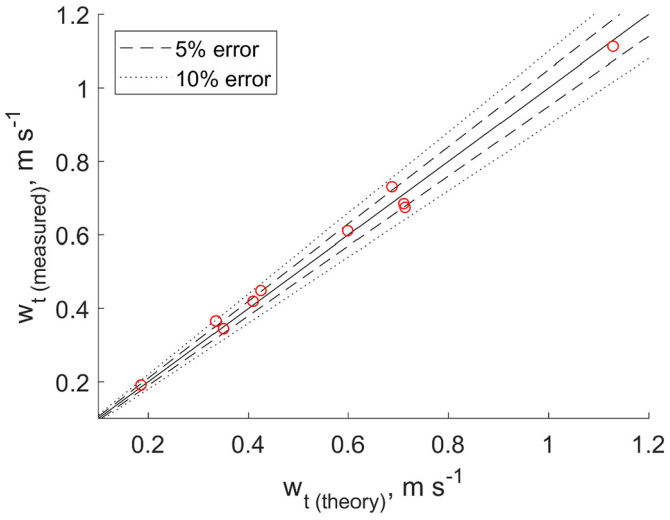

Fig. 2. Measurements of w_t for spheres (this study), compared with the analytical solution of White (1974). The solid line indicates perfect agreement between $w_{t\ (theory)}$ and $w_{t\ (measured)}$. Symbols show the mean of 5 repeat measurements. Standard errors are smaller than markers.

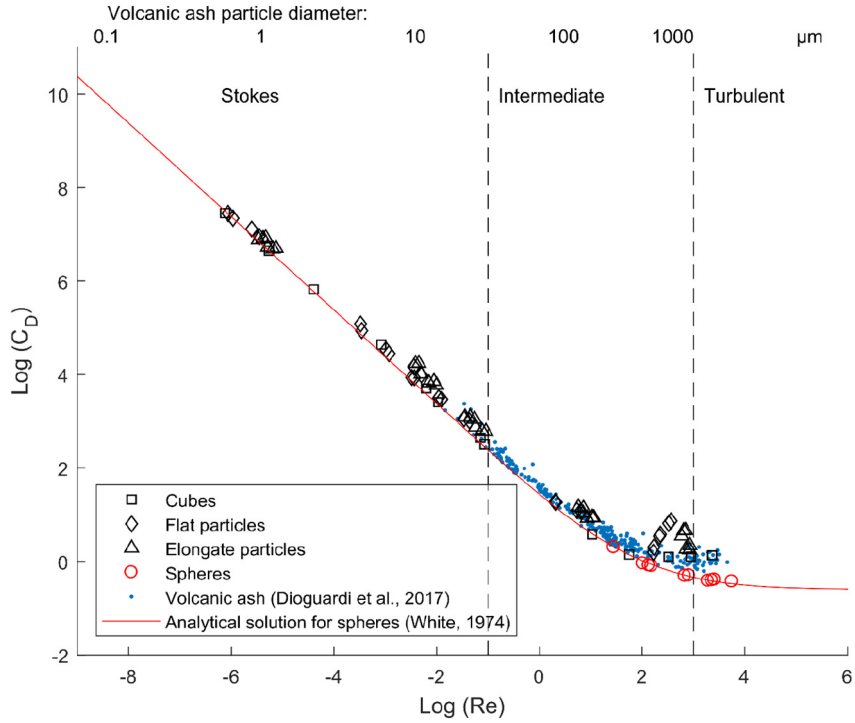

Fig. 3. Re – drag relationship for spheres (red line = theory, open circles = analogue experiments) compared to non-spherical analogues (this study) and volcanic ash (Dioguardi et al., 2017). Flow regime boundaries are shown using dashed lines. The upper x axis shows volcanic ash diameters plotted at their approximate corresponding Re, calculated using the White (1974) scheme with particle density = 2300 kg m^{-3}, air density = 1.225 kg m^{-3} and air viscosity = 1.983×10^{-5} Pa·s.

tumbling or oscillating motions, which depend on shape (Christiansen and Barker, 1965; Wilson and Huang, 1979) and particle-fluid density ratio (Chow and Adams, 2011; Bagheri and Bonadonna, 2016).

High drag coefficients relative to spheres mean that our non-spherical analogues fell up to ~75% slower (Fig. 4) than an analytical solution for spheres (White, 1974). Deviation from sphere velocity is greater at higher Re and lower sphericity. There is no marked difference between flat and elongate particles of equivalent Re; however, equant particles are a better fit to a spherical solution than either elongate or flat particles. Some equant particles appear to fall faster than equivalent-volume spheres; this is likely to be a result of raw measurement error on the velocity data, which we estimate to be on the order of 8% of $w_{t(theory)}$.

Formulae in which C_D is derived as a function of one or more geometric shape descriptors (Wilson and Huang, 1979; Ganser, 1993; Bagheri and Bonadonna, 2016; Dioguardi et al., 2017) in general provide

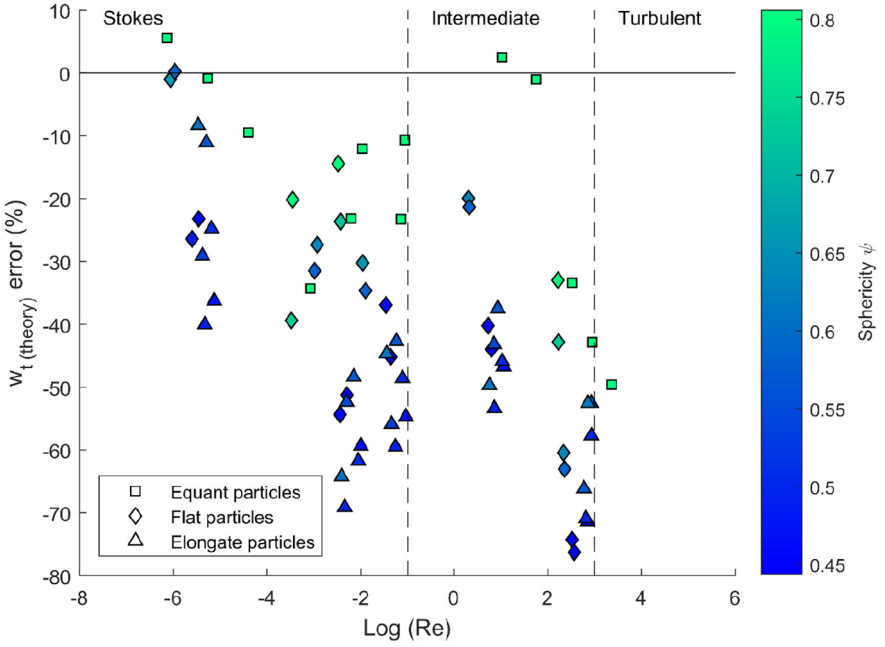

Fig. 4. Error in predicted terminal fall velocity for the White (1974) analytical solution, as a function of Re. Symbols indicate particle shapes; colours indicate particle sphericity. Negative values of $w_{t\ (theory)}$ error indicate that the scheme has overestimated terminal velocity.

a more accurate estimate of w_t (Fig. 5), although the predictions are still, on average, slight overestimations. The exception is that elongated particles can fall >1.5× faster than predicted by the w_t solution of Wilson and Huang (1979) within the Re range of their experiments, and >5.5× faster in Stokes flow (Fig. 5a).

Using the Ganser (1993) sedimentation scheme with the shape descriptor ψ_R (2D sphericity; Riley et al., 2003) in place of ψ (3D sphericity; Ganser, 1993) resulted in an increased range in error caused by an underestimation of terminal velocity for elongate particles and an overestimation for flat particles (Fig. 5d). For our elongate analogue particles $\psi_R < \psi$; the converse is true for flat particles. For volcanic ash particles, the ratio of ψ to ψ_R is complicated by morphological factors other than elongation or flatness, such as small-scale surface roughness; it is therefore important to assess the impact of quantifying ash shape in 2D, and in Section 4 we report ψ and ψ_R for two samples of volcanic ash.

The Ganser (1993) sedimentation scheme (using ψ; Fig. 5e) produced an overall mean absolute percentage error of 19%, which is comparable to the 16% error calculated from a larger compilation of data by Chhabra et al. (1999). We use the Ganser (1993) formula for the dispersion modelling in this study as it produces the lowest mean error of any scheme. However, we note that the Bagheri and Bonadonna (2016) formula produces similar results (mean absolute percentage error 26%, although less evenly distributed around zero) and is also valid for a wide Re range, due to the wide range of flow conditions and particle shapes used to produce the correlation and the semi-empirical construction of the formula.

4. Quantifying volcanic ash shape

We measured the shape of samples of SILK-LN and Vedde ash from Katla volcano, Iceland (Fig. 1). Both samples are tephra fall deposits collected from soil sections in Iceland, and so cannot be classified as distal ash fall, which is the focus of this study; however, we sieved the samples to extract grains of 62.5–125 μm for shape analysis, to allow comparison between samples with different PSDs for a size fraction representative of distal ash (Stevenson et al., 2015), noting that ash shape in a single size class can vary with distance from source (Þorsteinsdóttir, 2015).

4.1. 2D shape analysis using scanning electron microscopy (SEM)

We measured ψ_R from 2D images taken at the University of Bristol using a Hitachi S-3500 N scanning electron microscope (SEM). We obtained backscattered electron (BSE) images using variable pressure (VP) mode at a pressure of 40 Pa. Grids of 49 images were acquired for each sample, giving 800–1600 grains. Grains were manually separated on the slides, and have a tendency to rest with the maximum projected area in view; however we cannot discount grain overlap and particle orientation as sources of error in this technique. Subsequent shape analysis was carried out using ImageJ. We used manual thresholding to create binary images, followed by the Analyse Particles plugin to output raw shape data such as particle perimeter (P_p) and projected area (A_{proj}). We excluded particles with $A_{proj} < 750$ pixels as lower pixel counts can reduce the accuracy of perimeter measurements and strongly alter the particle's apparent morphology (Liu et al., 2015). We then calculated ψ_R using $\psi_R = 4\pi A_{proj}/P_p^2$ (Riley et al., 2003).

4.2. 3D shape analysis using X-ray computed microtomography (CT)

We measured ψ using 3D volumes obtained by CT scans carried out using a Nikon XTH225ST scanner at the University of Bristol. We carried out scans at a voxel (volumetric pixel) edge length of 3.5 μm, a voltage of 100 kV and a current of 70 μA.

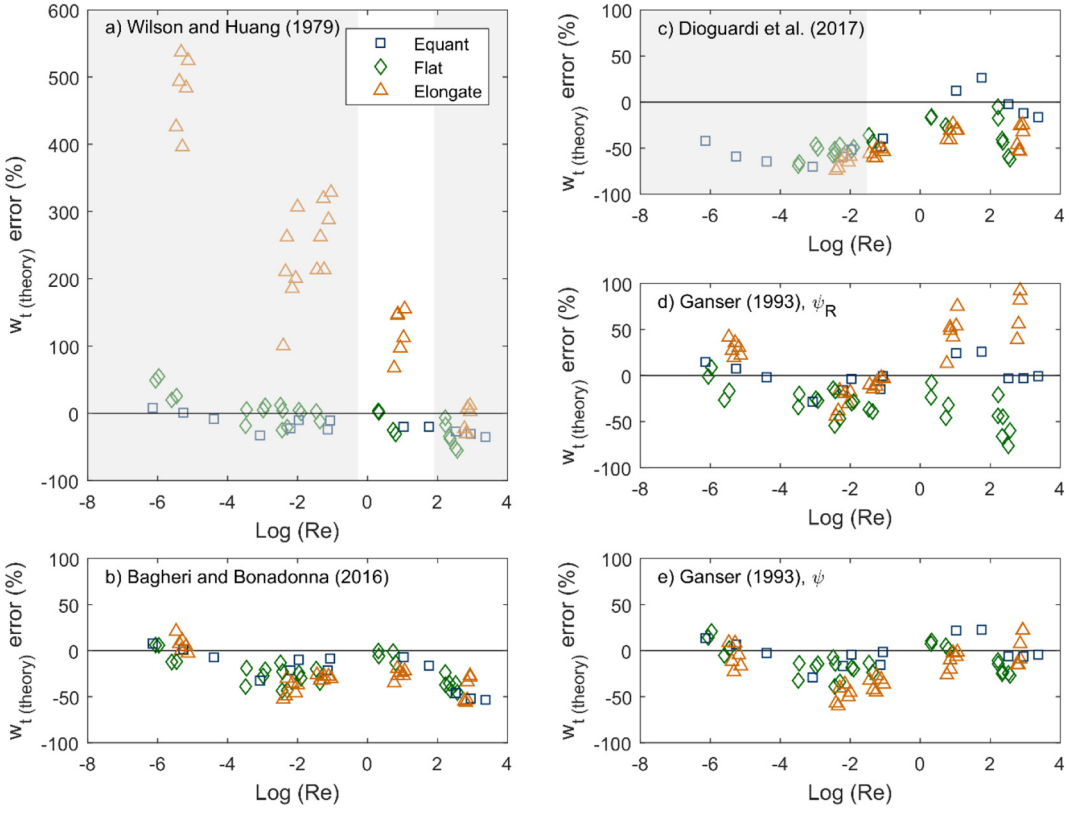

Fig. 5. Error in predicted terminal fall velocity for the various sedimentation schemes investigated, as a function of Re. Mathematical descriptions of sedimentation schemes are given in Table 2. Negative values of $w_{t\ (theory)}$ error indicate that the scheme has over-predicted terminal velocity. Greyed out areas indicate that measured Re is outside the range used to develop the correlation.

In CT analysis, samples are placed on a rotation table between an X-ray source and a detector. X-ray projections are taken as the sample is rotated from 0 to 360°; we used a rotation step of 0.11° giving 3141 projected images. The resulting images show density contrasts in the form of differing grey values in each voxel. To scan many particles efficiently, we encased the particles in epoxy resin, which ensured that particles were separated and did not move relative to each other during stage rotation. We filled 6 mm × 20 mm plastic cylinders with resin, waited 5–10 min for the resin to begin hardening, and then stirred in a weighed amount of ash sample, leaving the resin to completely set (~ 24 h) before scanning. The resin and plastic have lower X-ray attenuation coefficients than the ash, making it easy to segment the output 3D volume. In this way we were able to scan >100 particles for each sample in ~2.5 h.

The raw data, in the form of 2D projections, were reconstructed to 3D volumes using CT Pro 3D reconstruction software. We carried out particle edge detection and surface reconstruction in Avizo 3D image analysis software based on voxel grey value contrasts. We calculated surface area A_p and volume V_p for each object using Avizo's Label Analysis module on the segmented volume. We then calculated ψ using $\psi = \pi^{\frac{1}{3}}(6V_p)^{\frac{2}{3}}/A_p$ (Ganser, 1993).

To validate this procedure, we conducted a sensitivity analysis to assess the impact of resolution on shape analysis. We used progressive downsampling of the dataset (e.g. Liu et al., 2015) to artificially decrease the resolution, followed by a repetition of the Label Analysis step. We found that mean sample ψ fluctuates significantly at <1200 voxels/particle. A voxel edge length of 3.5 μm gives a minimum of 2800 voxels/particle for the samples analysed, indicating that our imaging resolution is sufficient.

4.3. Volcanic ash shape data

The shape distributions of the SILK-LN and Vedde ash samples are shown in Fig. 6. Both samples show a wide range of shapes within a single size class. Both ash samples are characterised by a low median ψ (0.53 for the SILK-LN ash and 0.52 for the Vedde ash), meaning that the particles are highly non-spherical. We used $\psi = 0.5$ for the dispersion modelling in the following section. Median ψ_R for both samples is within 0.1 of median ψ. ψ_R is lower than ψ for the SILK-LN ash at 0.44, and higher for the Vedde ash at 0.58. For both samples particle long axis L, from CT data, is on average twice the length of equivalent-volume sphere diameter d_v, with a median L/d_v of 2.1 for the SILK-LN ash and 2.0 for the Vedde ash.

5. Sensitivity of dispersion model forecasts to particle shape

We used NAME to assess the sensitivity of ash dispersion forecasts to the shape factor assigned to the particles, using the median 3D sphericity of the SILK-LN and Vedde ash samples ($\psi = 0.5$). For all simulations we released ash from an eruptive source above the summit of Katla caldera, Iceland (63.6°N, 19.1°W) and used numerical weather prediction meteorological data from the Met Office's Unified Model (UM; Cullen, 1993) with a horizontal resolution of 25 km and a temporal resolution of 3 h. Model eruptions were initiated from 00:00 on 15th April 2010, when prevailing wind transported ash from Eyjafjallajökull volcano (24 km west of Katla) to northern Europe, causing major disruption to aviation (Budd et al., 2011). We modelled ash particles as spheres using the White (1974) analytical formula, and non-spheres using the Ganser (1993) empirical formula and $\psi = 0.5$. Note that for $\psi = 0.5$, particle size refers to equivalent-volume sphere diameter d_v. We assumed a plume height of 15 km, within the observed range for VEI 4 eruptions (Newhall and Self, 1982) and a particle density of 2300 kg m^{-3}. Additional model parameters are detailed in the following sections.

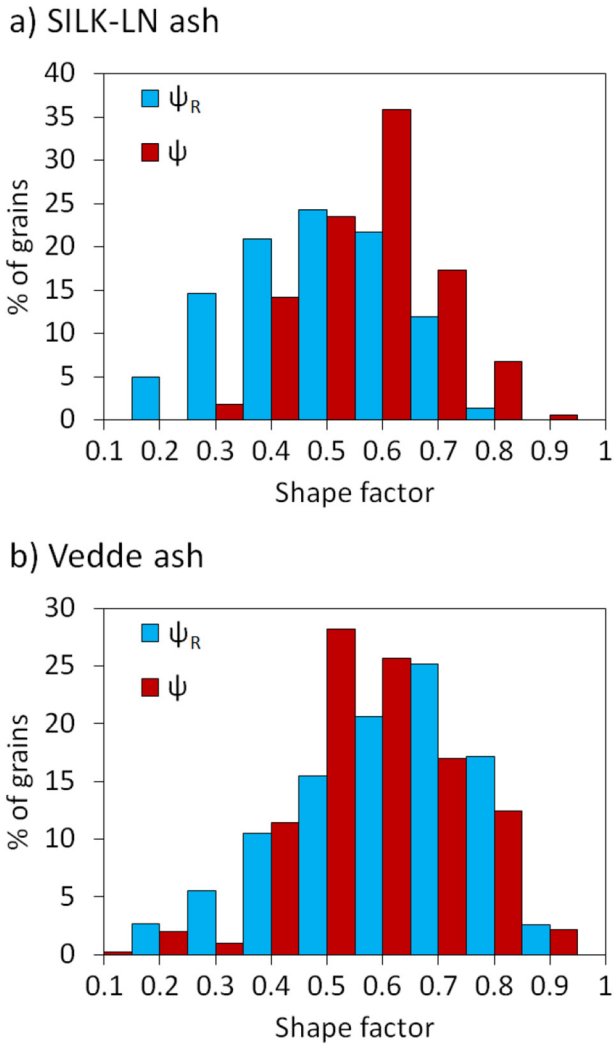

Fig. 6. Grain shape distributions of ψ and ψ_R for two samples of ash of 62.5–125 μm (sieve mesh size) from Katla volcano, Iceland: a) the SILK-LN ash and b) the Vedde ash.

5.1. Sensitivity of vertical velocity

The vertical velocity of particles in the atmosphere (w) is governed by sedimentation (w_{sed}) and atmospheric processes (w_a, w′); see Eq. (1). w_{sed} is sensitive to particle properties, including shape. Eq. (1) therefore suggests that w will be sensitive to particle shape where $w_{sed} \gg w_a + w'$. We evaluated the relative contribution of atmospheric vertical velocities to determine the conditions under which vertical velocity is sensitive to shape.

To assess the likely range of vertical wind velocity across northern Europe, we extracted w_a from the UM data for a region extending from Iceland to the UK and Scandinavia for 59 vertical model levels at 3 h intervals throughout April 2010. For example, Fig. 7 shows vertical air velocities at 6400 m asl. Vertical air velocities are mostly on the order of ±0.001 to ±0.1 m s^{-1}, with extremes around ±1 m s^{-1} (where +/− refers to up/down). UM vertical velocities are terrain following. However, to assess vertical velocities at altitude it is misleading to consider rate of change with respect to ground level, as the coordinate system will give a false impression of the terrain effect; we therefore present vertical velocities with respect to sea level.

Turbulence w′ fluctuates at sub-grid spatial and temporal scales and is difficult to anticipate. Therefore, dispersion models often use probability distributions to parameterise unresolved turbulence. In NAME,

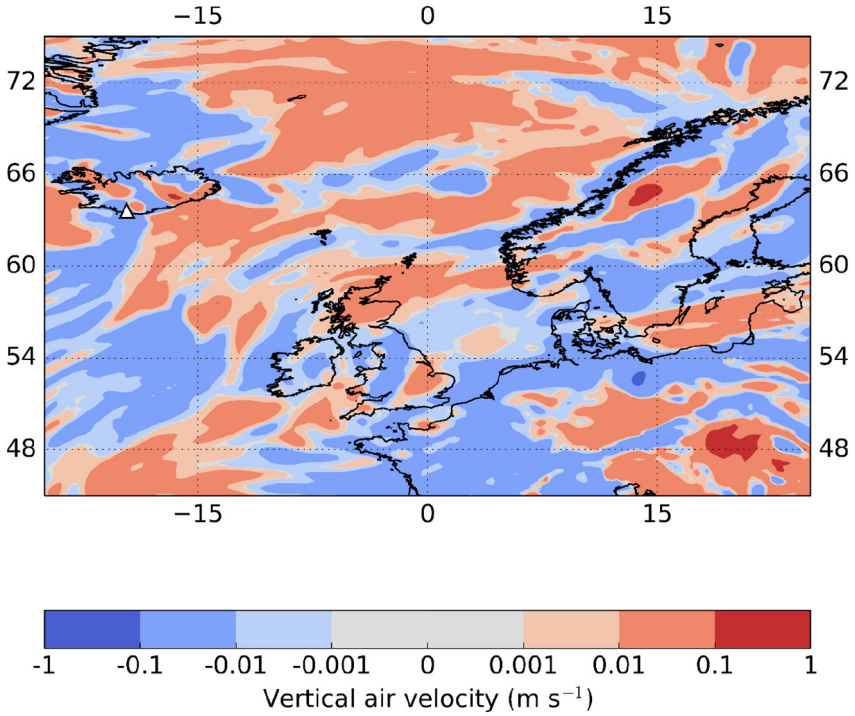

Fig. 7. Vertical wind velocities at 06:00 on 2010/04/14 at Unified Model level 30 (altitude 6400 m, bounds = 6196.66, 6610.0). White triangle shows the position of Katla volcano in south Iceland.

the vertical component of turbulence is time-averaged and a function of the random component r:

$$w' = \sqrt{\frac{2\kappa}{\Delta t}}\, r, \tag{5}$$

where Δt is the model timestep (s), κ is turbulent diffusivity, and r has a mean of 0 and a variance σ^2 of:

$$\sigma^2 = \frac{2\kappa}{\Delta t}. \tag{6}$$

Turbulent diffusity κ is calculated by $\sigma^2\tau$, where τ is the rate of dissipation of turbulent kinetic energy. Where sedimentation of heavy particles is modelled, κ is reduced according to settling velocity to account for particles falling through turbulent eddies (Maryon et al., 1999) and can be calculated by:

$$\kappa = {\sigma_w}^{*2}{\tau_w}^{*}, \tag{7}$$

where the subscript w denotes the vertical and

$${\tau_w}^{*} = \frac{\tau_w}{\sqrt{1 + {w_t}^2/{\sigma_w}^2}}, \tag{8}$$

$${\sigma_w}^{*} = \frac{\sigma_w}{\sqrt{1 + T_p/{\tau_w}^{*}}}, \tag{9}$$

and T_p is the particle time constant (Maryon et al., 1999):

$$T_p = \frac{w_t}{g}\,\frac{\rho_p - \rho}{\rho_p} \tag{10}$$

In the free troposphere (above the boundary layer), vertical turbulence parameters are assumed to be constant at $\tau_w = 100$ s and $\sigma_w = 0.1$ m s^{-1} (Jones et al., 2015).

As turbulence in NAME is timestep-dependent, we cannot directly compare w′ and w_{sed}. We instead compared time for a particle to deposit due to sedimentation alone (T_{sed}) to time taken for the same particle to reach the ground through turbulent diffusion alone (T_{diff}), where:

$$T_{sed} = \frac{H}{w_t}, \tag{11}$$

and H is plume height, and

$$T_{diff} = \frac{H^2}{\kappa}. \tag{12}$$

We calculated the ratios w_{sed}/w_a and T_{diff}/T_{sed} for particles of 0.1–100 μm assuming $\rho_P = 2300$ kg m^{-3}, $\rho = 1.225$ kg m^{-3}, and $\mu = 1.98 \times 10^{-5}$ Pa·s. We used NAME to simulate ash dispersal from an eruption of Katla volcano, Iceland, using a point source at 11490 m asl (10 km above summit and 5 km below our estimated plume height for the SILK-LN eruption).

5.1.1. Vertical velocity data

Ratios of particle sedimentation velocity to atmospheric velocity are shown in Fig. 8. Sedimentation has a greater impact on velocity than vertical wind advection where $w_{sed} > w_a$, and this is the case for particles of $d_v > 3$ to 100 μm depending on w_a (Fig. 8a). Sedimentation is more important than atmospheric turbulence where $T_{sed} < T_{diff}$. If we consider particle release heights between 5 and 25 km, $T_{sed} < T_{diff}$ for particles of minimum d_v ~1 μm (Fig. 8b). We conclude that vertical velocity w is significantly modified by w_{sed}, a function of particle shape, for particles larger than ~1–3 μm.

The results shown in Fig. 8 neglect the impact of boundary layer turbulence (Jones, 2004; Stull, 2012) on particle transport, and consider advection data for a limited period; a longer analysis may have given a wider range of velocities. However, the results remain valid when using a full atmospheric model. For example, Fig. 9 shows NAME modelled vertical trajectories of spherical and non-spherical particles of $d_v = 1$, 10 and 100 μm for the first 140 h after release. There is no discernible difference in the vertical trajectories of spherical and non-

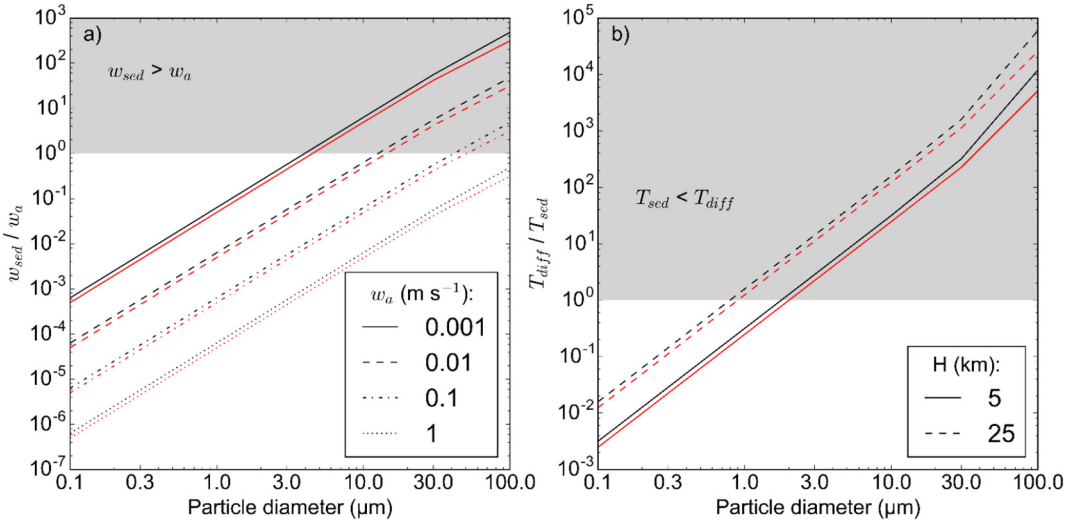

Fig. 8. a) Velocity ratio w_{sed}/w_a, and b) time ratio T_{diff}/T_{sed}, as a function of particle diameter. Diameters here are equivalent-volume sphere diameters (d_v). Black lines indicate spheres and are calculated using the White (1974) sedimentation scheme; red lines indicate $\psi = 0.5$ and are calculated using the Ganser (1993) sedimentation scheme.

spherical particles of $d_v = 1$ μm. There is a significant vertical spread between individual trajectories, and particles move in both the positive and negative direction, suggesting transport is dominated by advection and turbulent diffusion; sedimentation velocity is always positive. The vertical position of $d_v = 10$ μm particles is slightly sensitive to shape, but they still exhibit both upward and downward motion. For $d_v = 100$ μm particles there is a clear vertical separation between the trajectories of spherical and non-spherical particles and the time taken for particles to sediment is well predicted by T_{sed} alone, suggesting $w_{sed} > w_a + w'$. As w_{sed} is a function of shape, it is important to quantify shape for particles of $d_v = 100$ μm where we need an accurate assessment of particle travel time.

5.2. Sensitivity of particle travel distance

To assess the maximum travel distance of individual particles, we carried out NAME runs with single particle sizes >100 μm, the maximum size used by the London VAAC. We used a 1D eruptive source based on a uniform distribution of particles from vent height to plume top.

5.2.1. Particle travel distance data

Maximum travel distance of particles >100 μm is sensitive to shape (Fig. 10), with non-spherical particles travelling 44% further for a $d_v = 100$ μm particle and 87% further for a $d_v = 500$ μm particle. Although most VAACs assume that particles of $d_v > 100$ μm fall out close to source (Hort, 2016), in the meteorological conditions simulated here, a $d_v = 200$ μm and $\psi = 0.5$ particle can travel 528 km and a $d_v = 300$ μm particle of the same shape can travel 360 km from source. The travel distances for equivalent-volume spheres are 336 km and 216 km respectively.

5.3. Sensitivity of atmospheric ash loading

We used NAME to model an eruption of Katla volcano using parameters estimated for the eruption of the SILK-LN tephra. To calculate mass flow rate and duration, we used the Mastin et al. (2009) correlation between plume height and erupted mass $H = 2V^{0.241}$, where H is plume height in km, V is volumetric flow rate in m^3 s^{-1} and volume is given as dense rock equivalent (DRE). An eruption duration of 7.8 h and a mass flow rate of 3.54×10^{13} g h^{-1} gives the total estimated tephra volume (0.12 km^3 DRE; Larsen et al., 2001). We assumed that 95% of erupted mass is deposited close to source (Rose et al., 2000, 2001; Webster et al., 2012; Dacre et al., 2013), and multiplied the mass flow rate by a distal fine ash fraction of 5% to give an effective source of 1.77×10^{12} g h^{-1}. We distributed this mass over 15,000 model particles released per hour, the particle release rate used by the London VAAC (Witham et al., 2017).

As particles larger than the London VAAC's default maximum size of $d_v = 100$ μm can travel sufficiently far to be relevant for distal ash dispersal where shape is non-spherical (Fig. 10), we used both the London VAAC default PSD (Maryon et al., 1999) and an additional coarser PSD, which we term the Katla SILK PSD (Fig. 11). The Katla SILK PSD was derived from an average of 19 sieved and weighed samples of Katla SILK-LN tephra (data from Þorsteinsdóttir, 2015), which we normalised to a size range of 0.09–250 μm. The London VAAC default PSD uses grain sizes based on light scattering (Hobbs et al., 1991), and the Katla SILK PSD uses sieve mesh sizes (Þorsteinsdóttir, 2015), whereas the sedimentation equations in NAME use d_v; we therefore make the simplifying assumption that scattering size ≈ sieve size ≈ d_v for the purpose of this sensitivity analysis.

To produce ash loading forecasts, we output volcanic ash air concentrations (g m^{-3}) at 22 vertical flight levels of 25 FL (2500 ft) depth and vertically integrated total column mass (g m^{-2}) over six 6-h averaged time periods. We then extracted the spatial extent of concentrations exceeding an 'unsafe to fly' threshold of $>2 \times 10^{-3}$ g m^{-3} based on aircraft encounters with volcanic ash (Clarkson et al., 2016). For total column mass we took an equivalent concentration of >2 g m^{-2} to be 'unsafe' assuming the plume is 1 km thick, a reasonable value for moderate Icelandic eruptions (e.g. Dacre et al., 2013). We then assessed the percentage overlap of 'unsafe' concentrations for spherical and non-spherical cases. We limited our analysis to model levels and timesteps where at least 100 grid cells contain 'unsafe' concentrations. As a statistical measure, percentage overlap of a concentration contour has the advantage of reflecting differences in both the spatial position of the plume and the magnitude of the ash concentration values.

5.3.1. Ash loading forecast data

The percentage overlap between model ash concentrations of spherical and non-spherical ($\psi = 0.5$) particles decreases with time after the eruption start (Fig. 12a). Modelled concentrations are more sensitive to sphericity when we use the coarser Katla SILK PSD: using the London VAAC default PSD, the mean percentage overlap for total column mass loading in the first 36 h after eruption is 95%, whereas for the Katla SILK PSD it is 87%. The lowest total column mass overlaps are 89% and 64%, respectively, representing good agreement between the spherical and non-spherical models even when using a coarser PSD (Fig. 12c–

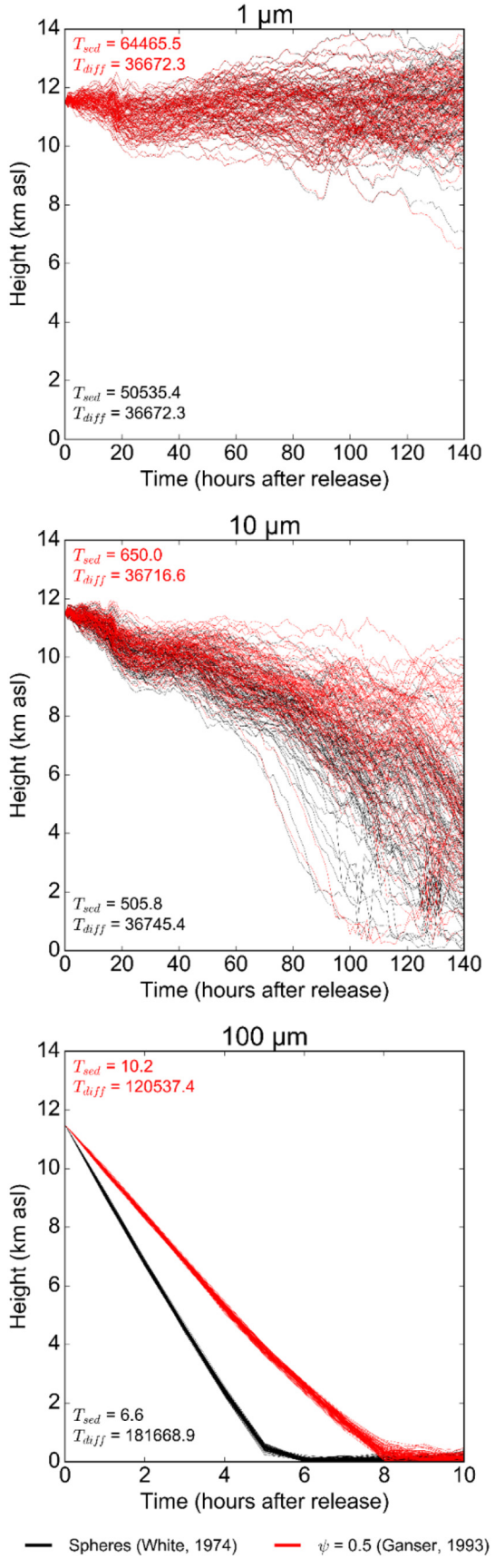

Fig. 9. Calculated trajectories of spherical (black) and non-spherical (red) particles of 1, 10 and 100 μm. Diameters here are equivalent-volume sphere diameter (d_v). Diffusion time T_{diff} and sedimentation time T_{sed} are calculated using Eqs. (11)–(12).

d). Air concentrations are more sensitive to shape than total column mass loading (Fig. 12b), suggesting that the vertical structure of the distal ash cloud is more sensitive to particle shape than the horizontal extent. Fig. 12b shows the model timestep and vertical level which are most sensitive to shape (49% overlap); the mean for air concentration forecasts is much higher at 87%, meaning that the spherical and non-spherical models agree reasonably well for most vertical levels and timesteps.

6. Discussion

Irregular shapes have higher drag coefficients (C_D) and lower terminal velocities (w_t) than equivalent-volume spheres. Our non-spherical analogue particles fall up to ~75% slower than an analytical solution for w_t of spheres (White, 1974). Empirical sedimentation schemes for non-spherical particles generally produce lower errors; the schemes of Ganser (1993) and Bagheri and Bonadonna (2016) are particularly effective. The Ganser (1993) scheme is calibrated using 3D sphericity ψ but often used with 2D sphericity ψ_R; we find that $\psi > \psi_R$ for elongated grains and $\psi < \psi_R$ for platy grains. Both the Katla tephras (SILK-LN and Vedde) have a median $\psi \approx 0.5$; using this value as a shape parameter in the NAME atmospheric dispersion model causes particles to travel further than equivalent-volume spheres. However, the sensitivity of atmospheric dispersion predictions to shape is dependent on the particle size modelled, as the transport of particles with $d_v < 1$–3 μm is primarily governed by atmospheric vertical velocities (wind advection w_a and turbulence w′) rather than sedimentation velocity w_{sed}, which is a function of shape. Particles of up to $d_v \approx 100$ μm are still affected by w_a and w′, although to a lesser extent. Therefore, there is relatively good agreement between distal ash concentration forecasts using spherical and non-spherical particle models when a significant proportion of particles are <100 μm. However, it is necessary to use a shape parameter when modelling larger particles, for example proximal and medial tephra dispersion or tephra fallout applications.

In the following sections we discuss some of the implications and caveats of these conclusions. First we assess the use of scaled analogue particles as an experimental tool and discuss reasons for the relative success of the empirical sedimentation schemes and shape factors used to predict w_t. We then discuss ash shape data for the SILK-LN and Vedde samples with implications for how we measure volcanic ash shape, and how our particle size measurements also depend on shape. We conclude by discussing implications of the sensitivity of dispersion models to shape from points of view of both operational concentration forecasting and cryptotephra dispersal.

6.1. Shape and sedimentation schemes

The use of scaled analogue particles allows us to systematically vary Re and easily measure shape; however, the analogues we use are simplified versions of volcanic ash particles. Volcanic ash particles can contain many small bubbles and have rough surfaces. In the Stokes regime, C_D is insensitive to surface roughness (Loth, 2008). However, in the turbulent regime, increasing roughness results in higher C_D (Achenbach, 1974), although this effect is small compared to particle shape (Bagheri and Bonadonna, 2016). If bubble size is large relative to particle size, or the bubble content is high, volcanic particles may be better approximated by hollow rather than solid shapes. Hollow objects permit the flow of fluid inside the object as well as around it; Chhabra et al. (1999) found that the Ganser (1993) sedimentation scheme could not accurately predict the velocities of particles in experiments with hollow cylinders and agglomerates (e.g. Lasso and Weidman, 1986). Another effect of bubbles and phenocrysts in volcanic particles is to move the particle's centre of mass from its geometric centre. In a non-equant particle, removing the centre of mass from the geometric centre can have a major effect on particle orientation (Tennant, 2017), and therefore projected area in the direction of fall, which is an important indicator

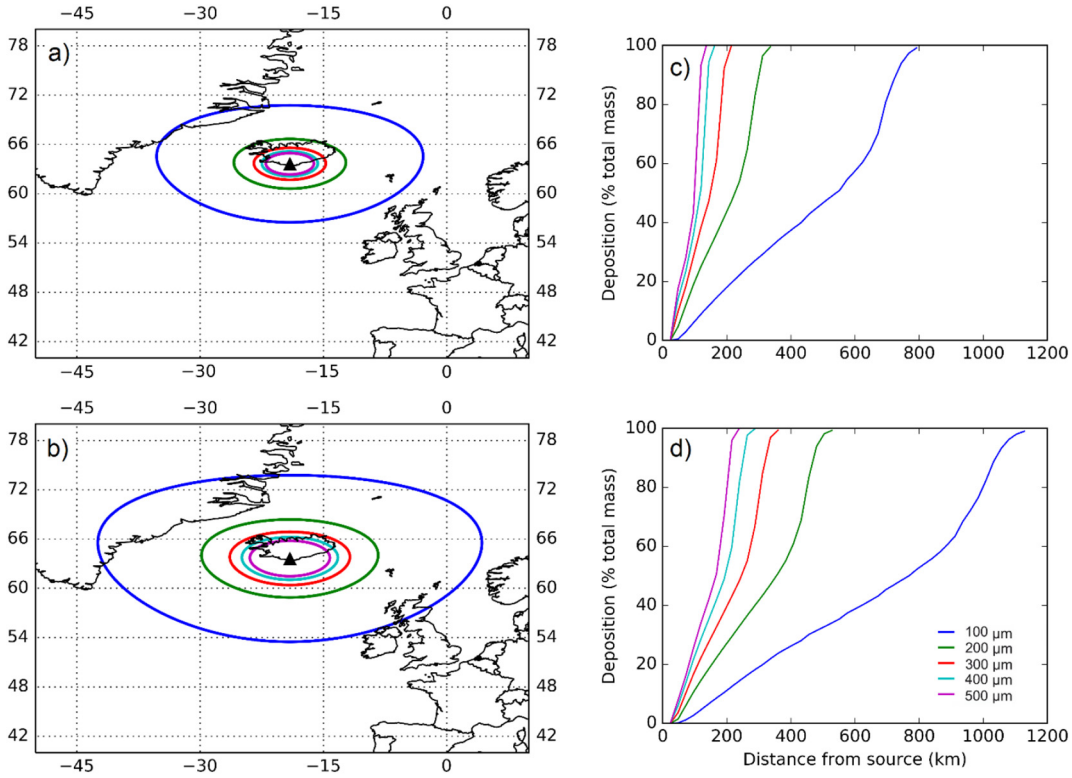

Fig. 10. The maximum travel distances of particles from Katla volcano, Iceland (black triangle) represented as great circle distances from the volcano and percentage deposited as a function of distance. a) maximum travel distance of spherical particles; b) maximum travel distance of non-spherical particles ($\psi = 0.5$); c) deposition vs distance for spherical particles; d) deposition vs distance for non-spherical particles ($\psi = 0.5$).

of C_D (Leith, 1987), especially for very non-spherical particles (Bagheri and Bonadonna, 2016).

Empirical formulae for irregular particles generally produce more accurate estimates of w_t than analytical formulae for spheres. However, the shape formulae of Wilson and Huang (1979) and Dioguardi et al. (2017) should only be used within $0.54 < Re < 79.1$ and $0.03 < Re < 10^4$ respectively, due to the uncertainty inherent in extrapolating empirical formulae beyond the Re range of the experiments used to produce the correlation. This highlights a limitation of experiments using ash particles, which cannot replicate the flow conditions of the smallest (lowest Re) particles falling in air.

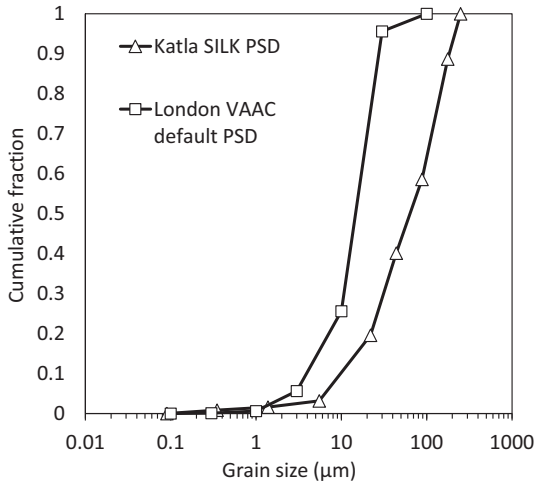

Fig. 11. Particle size distributions used to assess the sensitivity of ash loading forecasts to shape: the London VAAC default PSD (Maryon et al., 1999) and the Katla SILK PSD (modified from Þorsteinsdóttir, 2015).

While Wilson and Huang (1979) and Dioguardi et al. (2017) use volcanic ash particles, Ganser (1993) and Bagheri and Bonadonna (2016) use analogue particles. The schemes using analogue particles are calibrated over a much wider Re range but may not replicate the shape or particle-fluid density ratio of ash falling in air. The empirical scheme of Bagheri and Bonadonna (2016) addresses this problem by combining analogue particle data with volcanic ash data and calibrating the results using a wide range of particle-fluid density ratios. Considering this context, the poorer performance of the Wilson and Huang (1979) and Dioguardi et al. (2017) drag laws, even within their experimental Re ranges, relative to Bagheri and Bonadonna (2016) and Ganser (1993), can likely be explained by the differences in shape between the volcanic ash particles used to calibrate the laws and the smooth analogue particles of our database. The Dioguardi et al. (2017) experiments use ash particles with sphericity ψ of 0.07–0.732, whereas our analogues have ψ of 0.45–0.8. While the Dioguardi et al. (2017) scheme does not iterate to convergence for all particles outside their experimental Re range, the Wilson and Huang (1979) scheme iterates to convergence for all particles in this study but underestimates terminal velocity for elongate particles. We suggest that this is due to the shape descriptor used in the Wilson and Huang (1979) formula, given by $F = (I + S)/2L$, where L, I, and S are the long, intermediate and short particle axes respectively. The construction of the equation means F is very sensitive to the particle long axis L. For volcanic ash particles in Wilson and Huang (1979), F ranges from 0.13 to 0.86 with a mean of 0.41; for elongate analogues in this study, F ranges from 0.06–0.13. This highlights a difficulty in extrapolating empirical sedimentation schemes beyond the shape range used to produce the correlation, as well as beyond the Re range.

We used the Ganser (1993) sedimentation scheme for dispersion modelling due to the low mean terminal velocity error of 19%. However, the Bagheri and Bonadonna (2016) formula produces similar results (mean absolute percentage error 26%, a comparable result given our estimated ~8% error on measured terminal velocities) and is valid for a wide Re range; moreover, it uses two fitting parameters (flatness f

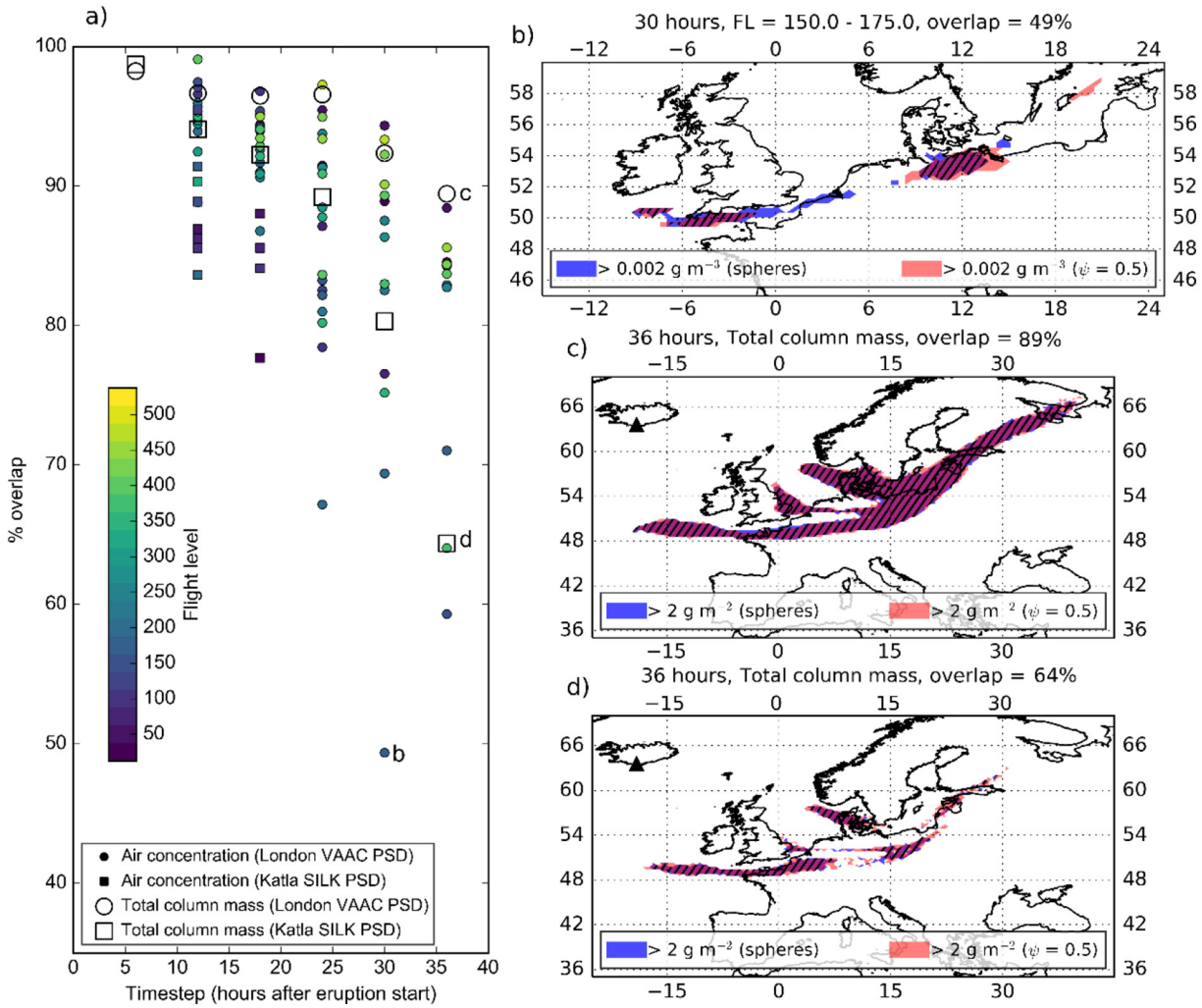

Fig. 12. a) The impact of particle shape on atmospheric ash loading, given as percentage overlap of the modelled ash cloud with spherical and non-spherical ($\psi = 0.5$) particles. Results are given for individual air concentrations corresponding to flight levels of 25 FL depth, and for total column mass (vertically integrated). Results plotted in panels b), c) and d) correspond to the symbols labelled with letters in panel a). b) The vertical position of ash particles can be sensitive to sphericity. c) Total column mass loading is relatively insensitive to sphericity. d) Using a coarser PSD (up to 250 μm) still results in low sensitivity of total column mass to sphericity in the first 36 h after eruption. Hatched areas indicate overlap. Black triangle indicates the source volcano (Katla, Iceland).

and elongation e; see Table 2) which are ratios of principal axis lengths and therefore less resolution-dependent than surface area-based measures such as ψ (Bagheri et al., 2015). Calculation of C_D using the Bagheri and Bonadonna (2016) formula requires particle-fluid density ratio, but knowledge of these properties is also required for the w_t calculation. We recommend that the Bagheri and Bonadonna (2016) scheme also be trialled as a volcanic ash dispersion modelling tool where it is more practical to obtain f and e rather than ψ.

6.2. Quantifying volcanic ash shape

The tephra layers sampled in this study were selected to examine the impact of characteristic non-equant particles (Larsen et al., 2001; Mangerud et al., 1984) on shape measurement and dispersion modelling. The SILK-LN and Vedde ash both have a median ψ of ~ 0.5. In comparison, Alfano et al. (2011) analysed ash grains from eruptions of several volcanoes (Masaya, Nicaragua; Kilauea, USA; and Soufriere Hills, Montserrat) and found that ψ ranged from 0.7–0.9, while ψ of ash particles from Campi Flegrei, Italy, ranges from 0.2–0.5 (Mele and Dioguardi, 2018). Thus, although the Katla SILK-LN and Vedde ash have similar median ψ, ash from other volcanoes can be of very variable morphology. Additionally, both Katla samples have a large ψ range, indicating that a single value of sphericity is not valid for each size class (see also Alfano et al., 2011 and Mele and Dioguardi, 2018). Average sphericity is also sensitive to the measurement technique (Alfano et al., 2011; this study).

The low sphericity of the measured ash particles has implications for how we measure particle size. Most sedimentation schemes assume size = d_v. However, the cryptotephra community usually reports size as maximum grain lengths, while volcanologists report particle size distributions in terms of sieve mesh sizes. For a sphere, the three measures are equivalent. For simplicity, we assume that for a non-spherical particle, maximum grain length = long axis L and sieve mesh size = intermediate axis I, that is, all particles with I < mesh size fall through the mesh. Fig. 13 illustrates the discrepancy between L, I and d_v for non-spheres. We show theoretical L and I for particles of d_v = 1–500 μm assuming particles are cylinders with $\psi = 0.5$; there are two cylinders with $\psi = 0.5$ for each d_v, one corresponding to an elongate cylinder (rod) and one corresponding to a flat cylinder (disk). The rod of d_v = 100 μm and $\psi = 0.5$ has L = 568 μm and I = 34.5 μm. The disk of d_v = 100 μm and $\psi = 0.5$ has L = 180 μm and I = 180 μm. Given the discrepancy between L and d_v, particle irregularity and the difference in size measurement conventions are likely to partially explain the inability of dispersion models to account for the travel distances of some large volcanic ash shards in cryptotephra deposits (Beckett et al., 2015; Stevenson et al., 2015; Watson et al., 2016), particularly given that

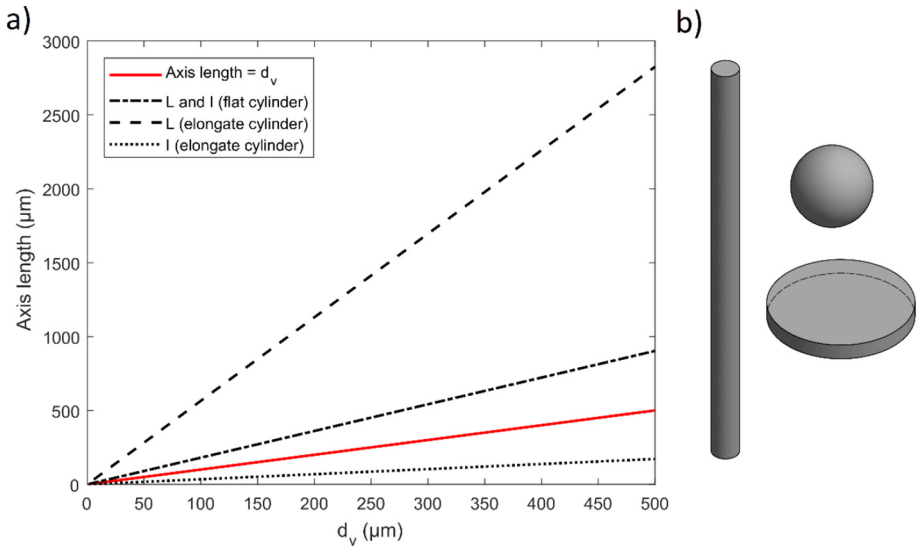

Fig. 13. a) Theoretical relationship of equivalent-volume sphere diameter d_v to long axis L and intermediate axis I for a cylinder of sphericity $\psi = 0.5$. For each dv there are two cylinders with $\psi = 0.5$; one a flat disk and one an elongate rod. b) Illustration showing a sphere and two cylinders of equivalent volume and $\psi = 0.5$.

volcanic ash travel distances are highly sensitive to particle size (Beckett et al., 2015). The maximum travel distance of a $d_v = 100$ μm and $\psi = 0.4$ particle, modelled using NAME, from the eruption of Eyjafjallajökull volcano in 2010 was 1375 km. Stevenson et al. (2012) describe a 100 μm particle from the same eruption in Lincolnshire, UK, 1646 km from source. However, Stevenson et al. (2012) measure diameter as L while the NAME sedimentation equations use d_v. Fig. 13 shows that for a cylindrical particle of $\psi = 0.5$ and L = 100 μm, d_v could be 18 or 55 μm. A NAME model ash particle with $d_v = 30$ μm, which lies between the two, can travel 4586 km from source (Beckett et al., 2015), further than the 1646 km travelled by the Lincolnshire particle. Although uncertainty in atmospheric, source, and other physical particle parameters could contribute to the discrepancy between observed and modelled particle travel distances, this suggests that the distance may be resolved solely by using a consistent size parameter from measurement to modelling.

6.3. Operational volcanic ash forecasting

Shape begins to influence particle trajectories at diameters between 1 and 100 μm, and becomes an important influence at $d_v > 100$ μm, the maximum diameter modelled by most VAACs (Hort, 2016). As non-spherical particles remain in the atmosphere longer than spheres, it is important to consider non-sphericity when assessing a suitable PSD for dispersion modelling. We show that a $d_v = 200$ μm non-spherical particle can travel >500 km from source, meaning that these particles have the potential to be present in a large region of airspace even after a moderate eruption (Fig. 10).

Despite the sensitivity of the travel distance of large particles to shape, we find that ash concentration forecasts for a model eruption of Katla volcano using NAME are relatively insensitive to shape even when we increase maximum d_v to 250 μm (Fig. 12). The vertical structure of the plume, however, as indicated by outputs on relatively thin vertical layers (25 FL depth), is more sensitive to shape. The lower sensitivity of total column mass loading to shape (Fig. 12c-d) is dependent on the input met data. If there is little vertical variation in wind speeds, different particle fall velocities will have less of an effect on horizontal dispersion than if winds at different altitudes are very different. Sensitivity to shape is also higher for larger particles, which is of concern for modelling proximal particle concentrations and tephra deposition. However, for operational scenarios, shape data are unlikely to be available in real-time. Currently, there are limited data on ash shape and how it varies with particle size, magma composition, eruption style or intensity, which makes it challenging to set defaults for a given volcano or eruption style. Therefore, in most cases the best option could be to assume a shape value which lies within the observed range for volcanic ash (as the Buenos Aires VAAC does), or to quantify uncertainty by using a non-spherical particle case as part of an ensemble forecast.

The London VAAC uses a model setup with layers of 25 FL depth, enabling it to represent observations of very thin ash layers in the atmosphere (e.g. Schumann et al., 2011; Devenish et al., 2012). However, the vertical resolution of the met data, the uniform mass distribution at source between the vent and plume height, and the random components of turbulence and mesoscale motions mean that model plumes in NAME are usually thicker (Devenish et al., 2012). To account for unresolved high ash concentrations in thin plumes, concentrations in thin layers are multiplied by a 'peak-to-mean factor' of 10 and combined into thick layers (FL000 to FL200, FL200 to FL350, and FL350 to FL550) where the maximum thin layer value is taken as the value of the thick layer (Witham et al., 2017). In this way, the London VAAC setup accounts for differences in the height and thickness of the plume relative to the model output, and is likely to at least partially mask the impact of particle shape on vertical plume structure. Therefore in practice, the difference in operational products with and without a shape parameter may be smaller than those of the 25 FL depth outputs shown here.

In the vertical, particle velocity in NAME is a function of the physical particle properties and meteorology. For the particle diameters considered by the London VAAC (0.1–100 μm), we expect the particle trajectories to follow the turbulent eddies, but inertial effects are not insignificant for larger particles. In NAME, the Lagrangian timescales and turbulent velocity variances are reduced according to settling velocity (Jones et al., 2015), to account for trajectory-crossing and inertial effects. By the particle drag coefficient we account for the impact of the flow on the particle, but not for the impact of the particle on the flow, a concept which is still poorly understood (Voth and Soldati, 2017). In addition, particles are assumed to disperse passively in the horizontal according to meteorological conditions. The extent to which particle shape might modify horizontal particle trajectories is unknown; non-spherical particles can fall according to trajectories which may be vertical but include particle rotation (Wilson and Huang, 1979) or have a horizontal component (Tennant, 2017).

Satellite retrieval constraints on volcanic ash transport can be used to validate and update dispersion model forecasts (Wilkins et al., 2016), retrieve physical particle properties (Francis et al., 2012) and determine ash emission rates to provide an updated source term (Stohl et al., 2011). The horizontal distribution of ash in a plume (i.e. total column mass) is relatively insensitive to shape (Fig. 12), meaning particle shape is unlikely to be a significant source of discrepancy between plume positions in satellite retrievals and dispersion modelling. However, satellite retrievals could underestimate ash concentrations where ash is extremely non-spherical because many scattering formulae assume spherical particles (e.g. Kylling et al., 2014), and satellite retrievals can detect only a limited range of particle sizes (Stevenson et al., 2015).

6.4. Beyond the days after eruption

Volcanic ash dispersion modelling for operational purposes is concerned with high atmospheric concentrations of ash hours to days after eruption (Folch, 2012), and satellite retrievals have difficulty detecting low concentrations and thin layers after the first few days of an eruption (Gangale et al., 2010). Our ash concentration sensitivity analysis is limited to a short timeframe of 36 h from eruption start. However, low concentrations of fine ash can remain in the stratosphere, influencing the atmospheric radiative budget, for months or years (Lacis et al., 1992; Gooding et al., 1983; Mackinnon et al., 1984). Critically, small reductions in gravitational settling velocity due to particle non-sphericity add up to greater differences in particle height (Fig. 9) and concentration (Fig. 12) over longer timeframes. Therefore, we cannot rule out shape as an influence on stratospheric ash loading over longer timescales (months to years), although shape is likely to be secondary to atmospheric controls on vertical velocity due to the small particle sizes (for example, a modal size of 2–5 μm and a maximum of 40 μm six months after the 1982 eruption of El Chichón; Gooding et al., 1983).

Understanding the long-term transport of ash has the potential to improve our understanding of cryptotephra deposits. Widely dispersed tephra from large eruptions can provide a linked age framework, up to continental scales, for host sediment sequences (e.g. Davies, 2015). Cryptotephra layers are usually correlated and linked to their source volcano by major and/or trace element analysis of glass shards (e.g. Tomlinson et al., 2015). Volcanic ash dispersion modelling could help to constrain potential source regions by providing estimates of maximum potential travel distances of the largest cryptotephra shards found in a site. We show that by using the same particle size parameter for ground-based sampling and dispersion modelling, we can better account for the particle sizes and travel distances reported in the two disciplines. We also show that to forecast the transport distances of very large distal ash shards requires a shape parameterisation: the maximum dispersal distance of ash shards with $d_v > 100$ μm is highly sensitive to shape (Fig. 10). We note that using ψ_R as a shape descriptor can significantly alter predicted analogue particle velocities compared to using ψ (Fig. 5). Therefore, by using consistent size and shape parameters to calibrate sedimentation schemes and measure volcanic ash shards, we can reduce the error in dispersion model predictions of particle travel distance.

Acknowledgements

This work was supported by the Natural Environment Research Council and the Met Office, UK, as well as the AXA Research Fund and a Royal Society Wolfson Merit Award (to K. Cashman). We would like to acknowledge Helen Webster for her insights into the turbulence parameterisation in NAME, and Tom Davies (University of Bristol) for his help with obtaining and processing tomography data. We also acknowledge Dave Thomson, Claire Witham, Andrew Jones, and the Atmospheric Dispersion and Air Quality research group (Met Office, UK) for their support with dispersion modelling. Thanks are due to Fabio Dioguardi and one anonymous reviewer for providing detailed and constructive reviews, and to Matt Hort for providing feedback on an earlier draft.

Appendix A. Boundary wall correction

For particles settling in a finite fluid, boundary wall proximity can affect Stokesian resistance (Brenner, 1962). The magnitude of boundary effects diminishes with increasing tube diameter to particle diameter ratio, and increasing Re (Chhabra et al., 1996). This means that the size of the vessel used in particle settling experiments can affect the results, although that effect is not well-constrained for non-spherical particles (Chhabra, 1995). Studies of the terminal velocity of irregular shapes generally make no correction for boundary effects (Christiansen and Barker, 1965), account for wall effects by conducting experiments in a variety of vessel sizes (Unnikrishnan and Chhabra, 1991), or by applying an analytical correction for spherical particles (Pettyjohn and Christiansen, 1948).

The wall correction for spheres at high Re can be calculated by

$$k = \left(1-\frac{A_s}{A}\right)\left(1-\frac{A_s}{2A}\right)^{0.5}, \tag{A.1}$$

where k is the ratio of w_t in the confined medium to w_t in an unbounded expanse, and A_s is the cross-sectional area of the sphere and A is the cross-sectional area of the tank (Di Felice et al., 1995; Chhabra et al., 1996). However, the wall factor is also a function of Re for a fixed A_S/A. Since experimental determination of wall factors is dependent on drag curves that are accurate to around 5% (Chhabra et al., 1996), a critical Re can be defined for each A_S/A, above which Eq. (1) is reliable. This critical value is that at which k is 95% of the value predicted by Eq. (1). Reference values based on experimental data are given by Chhabra et al. (1996).

For lower Re and irregular shapes, best fits can be calculated for each shape by assuming that k = f(Re, d/D, shape) where d is particle diameter and D is tank diameter (Chhabra, 1995). Re is not a significant variable at 95% confidence intervals for most shapes. For flat plates (disks and squares) and d/D < 0.32,

$$k = 1-1.7\left(\frac{d}{D}\right), \tag{A.2}$$

where d is diameter (disks) or diameter of an equal projected area circle (squares). For cylinders, the length to diameter ratio is important. For $0.03 < d_v/D < 0.5$,

$$\begin{aligned} k &= 1-1.33\left(\frac{d_v}{D}\right) && \left(\frac{L}{S}\right)<10, \text{ and} \\ k &= 1-3.58\left(\frac{d_v}{D}\right) && \left(\frac{L}{S}\right)>10 \end{aligned} \tag{A.3}$$

where d_v is the diameter of a volume-equivalent sphere. For rectangular prisms the experimental scatter is greater, but error is around 10% at the 90% confidence level. For $0.16 < d_v/D < 0.6$,

$$k = 1-1.42\left(\frac{d_v}{D}\right). \tag{A.4}$$

With the exception of long cylinders (L/S > 10), all shapes show smaller wall effects than for a volume-equivalent sphere.

For the data in this study, boundary effects were corrected using Eqs. (A.1)–(A.4). Boundary errors are similar to standard errors based on repeat measurements, with k ranging from 0.94–1.0 with a mean of 0.98. For particles in the Stokes regime, where boundary effects are greatest, k was calculated using Eqs. (A.2)–(A.4). For particles in the intermediate and turbulent regimes, k values were calculated based on

volume-equivalent spheres Eq. (A.1), due to uncertainty inherent in extrapolating Chhabra (1995)'s shape-based corrections to higher Re. For these particles, k was consistently close to 1 with a mean of 0.99.

References

Achenbach, E., 1974. The effects of surface roughness and tunnel blockage on the flow past spheres. J. Fluid Mech. 65 (1), 113–125.

Alfano, F., Bonadonna, C., Delmelle, P., Costantini, L., 2011. Insights on tephra settling velocity from morphological observations. J. Volcanol. Geotherm. Res. 208 (3–4), 86–98.

Bagheri, G., Bonadonna, C., 2016. On the drag of freely falling non-spherical particles. Powder Technol. 301, 526–544.

Bagheri, G.H., Bonadonna, C., Manzella, I., Vonlanthen, P., 2015. On the characterization of size and shape of irregular particles. Powder Technol. 270, 141–153.

Beckett, F.M., Witham, C.S., Hort, M.C., Stevenson, J.A., Bonadonna, C., Millington, S.C., 2015. Sensitivity of dispersion model forecasts of volcanic ash clouds to the physical characteristics of the particles. J. Geophys. Res. Atmos. 120 (22), 11636–11652.

Beckett, F., Kylling, A., Sigurðardóttir, G., Löwis, S.V., Witham, C., 2017. Quantifying the mass loading of particles in an ash cloud remobilized from tephra deposits on Iceland. Atmos. Chem. Phys. 17 (7), 4401–4418.

Blockley, S.P.E., Lane, C.S., Lotter, A.F., Pollard, A.M., 2007. Evidence for the presence of the Vedde Ash in Central Europe. Quat. Sci. Rev. 26 (25–28), 3030–3036.

Brenner, H., 1962. Effect of finite boundaries on the Stokes resistance of an arbitrary particle. J. Fluid Mech. 12 (01), 35–48.

Budd, L., Griggs, S., Howarth, D., Ison, S., 2011. A fiasco of volcanic proportions? Eyjafjallajökull and the closure of European airspace. Mobilities 6 (1), 31–40.

Cashman, K.V., Rust, A.C., 2016. Volcanic ash: generation and spatial variations. In: Mackie, S., Cashman, K., Ricketts, H., Rust, A., Watson, M. (Eds.), Volcanic Ash: Hazard Observation. Elsevier, Amsterdam, pp. 5–22.

Cheng, N.S., 2008. Formula for the viscosity of a glycerol−water mixture. Ind. Eng. Chem. Res. 47 (9), 3285–3288.

Chhabra, R.P., 1995. Wall effects on free-settling velocity of non-spherical particles in viscous media in cylindrical tubes. Powder Technol. 85 (1), 83–90.

Chhabra, R.P., Uhlherr, P.H.T., Richardson, J.F., 1996. Some further observations on the hindered settling velocity of spheres in the inertial flow regime. Chem. Eng. Sci. 51 (19), 4531–4532.

Chhabra, R.P., Agarwal, L., Sinha, N.K., 1999. Drag on non-spherical particles: an evaluation of available methods. Powder Technol. 101 (3), 288–295.

Chow, A.C., Adams, E.E., 2011. Prediction of drag coefficient and secondary motion of free-falling rigid cylindrical particles with and without curvature at moderate Reynolds number. J. Hydraul. Eng. 137 (11), 1406–1414.

Christiansen, E.B., Barker, D.H., 1965. The effect of shape and density on the free settling of particles at high Reynolds numbers. AICHE J. 11 (1), 145–151.

Clarkson, R.J., Majewicz, E.J., Mack, P., 2016. A re-evaluation of the 2010 quantitative understanding of the effects volcanic ash has on gas turbine engines. J. Aerosp. Eng. 230 (12), 2274–2291.

Clift, R., Gauvin, W.H., 1971. Motion of entrained particles in gas streams. Can. J. Chem. Eng. 49 (4), 439–448.

Clift, R., Grace, J.R., Weber, M.E., 2005. Bubbles, Drops, and Particles. Dover Publications Inc., New York.

Costa, A., Macedonio, G., Folch, A., 2006. A three-dimensional Eulerian model for transport and deposition of volcanic ashes. Earth Planet. Sci. Lett. 241 (3–4), 634–647.

Costa, A., Folch, A., Macedonio, G., Giaccio, B., Isaia, R., Smith, V.C., 2012. Quantifying volcanic ash dispersal and impact of the Campanian Ignimbrite super-eruption. Geophys. Res. Lett. 39 (10).

Cullen, M.J.P., 1993. The unified forecast/climate model. Meteorol. Mag. 122 (1449), 81–94.

Dacre, H.F., Grant, A.L., Johnson, B.T., 2013. Aircraft observations and model simulations of concentration and particle size distribution in the Eyjafjallajökull volcanic ash cloud. Atmos. Chem. Phys. 13 (3), 1277–1291.

D'Amours, R., Malo, A., Servranckx, R., Bensimon, D., Trudel, S., Gauthier-Bilodeau, J.P., 2010. Application of the atmospheric Lagrangian particle dispersion model MLDP0 to the 2008 eruptions of Okmok and Kasatochi volcanoes. J. Geophys. Res. Atmos. 115 (D2).

Davies, S.M., 2015. Cryptotephras: the revolution in correlation and precision dating. J. Quat. Sci. 30 (2), 114–130.

Dellino, P., Mele, D., Bonasia, R., Braia, G., La Volpe, L., Sulpizio, R., 2005. The analysis of the influence of pumice shape on its terminal velocity. Geophys. Res. Lett. 32 (21).

Devenish, B.J., Thomson, D.J., Marenco, F., Leadbetter, S.J., Ricketts, H., Dacre, H.F., 2012. A study of the arrival over the United Kingdom in April 2010 of the Eyjafjallajökull ash cloud using ground-based lidar and numerical simulations. Atmos. Environ. 48, 152–164.

Di Felice, R., Gibilaro, L.G., Foscolo, P.U., 1995. On the hindered settling velocity of spheres in the inertial flow regime. Chem. Eng. Sci. 50 (18), 3005–3006.

Dietrich, W.E., 1982. Settling velocity of natural particles. Water Resour. Res. 18 (6), 1615–1626.

Dioguardi, F., Mele, D., Dellino, P., Dürig, T., 2017. The terminal velocity of volcanic particles with shape obtained from 3D X-ray microtomography. J. Volcanol. Geotherm. Res. 329, 41–53.

Dioguardi, F., Mele, D., Dellino, P., 2018. A new one-equation model of fluid drag for irregularly shaped particles valid over a wide range of Reynolds number. J. Geophys. Res. Solid Earth 123 (1), 144–156.

Draxler, R.R., Hess, G.D., 1997. Description of the HYSPLIT4 Modeling System.

Folch, A., 2012. A review of tephra transport and dispersal models: evolution, current status, and future perspectives. J. Volcanol. Geotherm. Res. 235, 96–115.

Folch, A., Costa, A., Macedonio, G., 2009. FALL3D: a computational model for transport and deposition of volcanic ash. Comput. Geosci. 35 (6), 1334–1342.

Francis, P.N., Cooke, M.C., Saunders, R.W., 2012. Retrieval of physical properties of volcanic ash using Meteosat: a case study from the 2010 Eyjafjallajökull eruption. J. Geophys. Res. Atmos. 117 (D20).

Gangale, G., Prata, A.J., Clarisse, L., 2010. The infrared spectral signature of volcanic ash determined from high-spectral resolution satellite measurements. Remote Sens. Environ. 114 (2), 414–425.

Ganser, G.H., 1993. A rational approach to drag prediction of spherical and nonspherical particles. Powder Technol. 77 (2), 143–152.

Garboczi, E.J., Riding, K.A., Mirzahosseini, M., 2017. Particle shape effects on particle size measurement for crushed waste glass. Adv. Powder Technol. 28 (2), 648–657.

Giehl, C., Brooker, R.A., Marxer, H., Nowak, M., 2016. An experimental simulation of volcanic ash deposition in gas turbines and implications for jet engine safety. Chem. Geol. 461, 160–170.

Gooding, J.L., Clanton, U.S., Gabel, E.M., Warren, J.L., 1983. El Chichón volcanic ash in the stratosphere: particle abundances and size distributions after the 1982 eruption. Geophys. Res. Lett. 10 (11), 1033–1036.

Haider, A., Levenspiel, O., 1989. Drag coefficient and terminal velocity of spherical and nonspherical particles. Powder Technol. 58 (1), 63–70.

Hobbs, P.V., Radke, L.F., Lyons, J.H., Ferek, R.J., Coffman, D.J., Casadevall, T.J., 1991. Airborne measurements of particle and gas emissions from the 1990 volcanic eruptions of Mount Redoubt. J. Geophys. Res. Atmos. 96 (D10), 18735–18752.

Holmes, N.S., Morawska, L., 2006. A review of dispersion modelling and its application to the dispersion of particles: an overview of different dispersion models available. Atmos. Environ. 40 (30), 5902–5928.

Hort, M., 2016. VAAC Operational Dispersion Model Configuration Snap Shot, Version 2. Dispersion Modelling Workshop Final Report. National Oceanic and Atmospheric Administration (NOAA) Centre for Weather and Climate Prediction (NCWCP).

ICAO, 2012. Flight Safety and Volcanic Ash. Document 9974. International Civil Aviation Organization.

Jones, A., 2004. Atmospheric dispersion modelling at the Met Office. Weather 59 (11), 311–316.

Jones, A., Thomson, D., Hort, M., Devenish, B., 2007. The UK Met Office's next-generation atmospheric dispersion model, NAME III. Air Pollution Modeling and its Application XVII, pp. 580–589.

Jones, A., Wellings, J., Bedwell, P., 2015. User Guide for NAME. NAME III Document MD15/8 (version 3.0). Met Office, UK.

Kylling, A., Kahnert, M., Lindqvist, H., Nousiainen, T., 2014. Volcanic ash infrared signature: porous non-spherical ash particle shapes compared to homogeneous spherical ash particles. Atmos. Meas. Tech. 7 (4), 919–929.

Lacis, A., Hansen, J., Sato, M., 1992. Climate forcing by stratospheric aerosols. Geophys. Res. Lett. 19 (15), 1607–1610.

Lane, C.S., Blockley, S.P., Mangerud, J.A.N., Smith, V.C., Lohne, Ø.S., Tomlinson, E.L., Matthews, I.P., Lotter, A.F., 2012. Was the 12.1 ka Icelandic Vedde Ash one of a kind? Quat. Sci. Rev. 33, 87–99.

Larsen, G., 2000. Holocene eruptions within the Katla volcanic system, south Iceland: characteristics and environmental impact. Jökull 49, 1–28.

Larsen, G., Newton, A.J., Dugmore, A.J., Vilmundardottir, E.G., 2001. Geochemistry, dispersal, volumes and chronology of Holocene silicic tephra layers from the Katla volcanic system, Iceland. J. Quat. Sci. 16 (2), 119–132.

Lasso, I.A., Weidman, P.D., 1986. Stokes drag on hollow cylinders and conglomerates. Phys. Fluids 29 (12), 3921–3934.

Lawson, I.T., Swindles, G.T., Plunkett, G., Greenberg, D., 2012. The spatial distribution of Holocene cryptotephras in north-west Europe since 7 ka: implications for understanding ash fall events from Icelandic eruptions. Quat. Sci. Rev. 41, 57–66.

Leadbetter, S.J., Hort, M.C., 2011. Volcanic ash hazard climatology for an eruption of Hekla Volcano, Iceland. J. Volcanol. Geotherm. Res. 199 (3–4), 230–241.

Leadbetter, S.J., Hort, M.C., Jones, A.R., Webster, H.N., Draxler, R.R., 2015. Sensitivity of the modelled deposition of Caesium-137 from the Fukushima Dai-ichi nuclear power plant to the wet deposition parameterisation in NAME. J. Environ. Radioact. 139, 200–211.

Leith, D., 1987. Drag on nonspherical objects. Aerosol Sci. Technol. 6 (2), 153–161.

Liu, E.J., Cashman, K.V., Beckett, F.M., Witham, C.S., Leadbetter, S.J., Hort, M.C., Guðmundsson, S., 2014. Ash mists and brown snow: remobilization of volcanic ash from recent Icelandic eruptions. J. Geophys. Res. Atmos. 119 (15), 9463–9480.

Liu, E.J., Cashman, K.V., Rust, A.C., 2015. Optimising shape analysis to quantify volcanic ash morphology. GeoResJ 8, 14–30.

Loth, E., 2008. Drag of non-spherical solid particles of regular and irregular shape. Powder Technol. 182 (3), 342–353.

MacKinnon, I.D., Gooding, J.L., McKay, D.S., Clanton, U.S., 1984. The El Chichón stratospheric cloud: solid particulates and settling rates. J. Volcanol. Geotherm. Res. 23 (1–2), 125–146.

Mangerud, J., Lie, S.E., Furnes, H., Kristiansen, I.L., Lømo, L., 1984. A younger dryas ash bed in western Norway, and its possible correlations with tephra in cores from the Norwegian Sea and the North Atlantic. Quat. Res. 21 (1), 85–104.

Maryon, R.H., Ryall, D.B., Malcolm, A.L., 1999. The NAME 4 Dispersion Model: Science Documentation. Met Office Turbulence and Diffusion Note. Met Office, UK, p. 262.

Mastin, L.G., Guffanti, M., Servranckx, R., Webley, P., Barsotti, S., Dean, K., Durant, A., Ewert, J.W., Neri, A., Rose, W.I., Schneider, D., Siebert, L., Stunder, B., Swanson, G., Tupper, A., Volentik, A., Waythomas, C.F., 2009. A multidisciplinary effort to assign realistic source parameters to models of volcanic ash-cloud transport and dispersion during eruptions. J. Volcanol. Geotherm. Res. 186 (1), 10–21.

Matthews, N.E., Smith, V.C., Costa, A., Durant, A.J., Pyle, D.M., Pearce, N.J., 2012. Ultra-distal tephra deposits from super-eruptions: examples from Toba, Indonesia and Taupo Volcanic Zone, New Zealand. Quat. Int. 258, 54–79.

Mele, D., Dioguardi, F., 2018. The grain size dependency of vesicular particle shapes strongly affects the drag of particles. First results from microtomography investigations of Campi Flegrei fallout deposits. J. Volcanol. Geotherm. Res. 353, 18–24.
Newhall, C.G., Self, S., 1982. The volcanic explosivity index (VEI) an estimate of explosive magnitude for historical volcanism. J. Geophys. Res. Oceans 87 (C2), 1231–1238.
Óladóttir, B.A., Larsen, G., Thordarson, T., Sigmarsson, O., 2005. The Katla volcano S-Iceland: Holocene tephra stratigraphy and eruption frequency. Jökull 55, 53–74.
Pettyjohn, E., Christiansen, E.B., 1948. Effect of particle shape on free-settling rates of isometric particles. Chem. Eng. Prog. 44 (2), 157–172.
Reckziegel, F., Bustos, E., Mingari, L., Báez, W., Villarosa, G., Folch, A., Collini, E., Viramonte, J., Romero, J., Osores, S., 2016. Forecasting volcanic ash dispersal and coeval resuspension during the April–May 2015 Calbuco eruption. J. Volcanol. Geotherm. Res. 321, 44–57.
Riley, C.M., Rose, W.I., Bluth, G.J., 2003. Quantitative shape measurements of distal volcanic ash. J. Geophys. Res. Solid Earth 108 (B10).
Rose, W.I., Bluth, G.J.S., Ernst, G.G., 2000. Integrating retrievals of volcanic cloud characteristics from satellite remote sensors: a summary. Philos. Trans. R. Soc. Lond. A 358 (1770), 1585–1606.
Rose, W.I., Bluth, G.J., Schneider, D.J., Ernst, G.G., Riley, C.M., Henderson, L.J., McGimsey, R.G., 2001. Observations of volcanic clouds in their first few days of atmospheric residence: the 1992 eruptions of Crater Peak, Mount Spurr Volcano, Alaska. J. Geol. 109 (6), 677–694.
Schumann, U., Weinzierl, B., Reitebuch, O., Schlager, H., Minikin, A., Forster, C., Baumann, R., Sailer, T., Graf, K., Mannstein, H., Voigt, C., Rahm, S., Simmet, R., Scheibe, M., Lichtenstern, M., Stock, P., Rüba, H., Schäuble, D., Tafferner, A., Rautenhaus, M., Gerz, T., Ziereis, H., Krautstrunk, M., Mallaun, C., Gayet, J.-F., Lieke, K., Kandler, K., Ebert, M., Weinbruch, S., Stohl, A., Gasteiger, J., Groß, S., Freudenthaler, V., Wiegner, M., Ansmann, A., Tesche, M., Olafsson, H., Sturm, K., 2011. Airborne observations of the Eyjafjalla volcano ash cloud over Europe during air space closure in April and May 2010. Atmos. Chem. Phys. 11, 2245–2279.
Stevenson, J.A., Loughlin, S., Rae, C., Thordarson, T., Milodowski, A.E., Gilbert, J.S., Harangi, S., Lukács, R., Højgaard, B., Árting, U., Pyne-O'Donnell, S., MacLeod, A., Whitney, B., Cassidy, M., 2012. Distal deposition of tephra from the Eyjafjallajökull 2010 summit eruption. J. Geophys. Res. Solid Earth 117 (B9).
Stevenson, J.A., Loughlin, S.C., Font, A., Fuller, G.W., MacLeod, A., Oliver, I.W., Jackson, B., Horwell, C.J., Thordarson, T., Dawson, I., 2013. UK monitoring and deposition of tephra from the May 2011 eruption of Grímsvötn, Iceland. J. Appl. Volcanol. 2 (1).
Stevenson, J.A., Millington, S.C., Beckett, F.M., Swindles, G.T., Thordarson, T., 2015. Big grains go far: reconciling tephrochronology with atmospheric measurements of volcanic ash. Atmos. Meas. Tech. Discuss. 8 (1).
Stohl, A., Prata, A.J., Eckhardt, S., Clarisse, L., Durant, A., Henne, S., Kristiansen, N.I., Minikin, A., Schumann, U., Seibert, P., Stebel, K., Thomas, H.E., Thorsteinsson, T., Tørseth, K., Weinzierl, B., 2011. Determination of time- and height- resolved volcanic ash emissions and their use for quantitative ash dispersion modeling: the 2010 Eyjafjallajökull eruption. Atmos. Chem. Phys. 11 (9), 4333–4351.
Stull, R.B., 2012. An Introduction to Boundary Layer Meteorology. Vol. 13. Springer Science & Business Media, Berlin.
Tennant, E., 2017. Settling velocity measurements of volcanic ash analogue particles with a non-uniform density distribution. Master's dissertation. School of Earth Sciences. University of Bristol.
Thordarson, T., Larsen, G., 2007. Volcanism in Iceland in historical time: Volcano types, eruption styles and eruptive history. J. Geodyn. 43 (1), 118–152.
Þorsteinsdóttir, E.S., 2015. Grain characteristics of tephra from the subglacial SILK-LN Katla eruption ~3400 years ago and the subaerial Hekla eruption in 1947. Master's dissertation. Faculty of Earth Sciences, University of Iceland.
Tomlinson, E.L., Smith, V.C., Albert, P.G., Aydar, E., Civetta, L., Cioni, R., Çubukçu, E., Gertisser, R., Isaia, R., Menzies, M., Orsi, G., Rosi, M., Zanchetta, G., 2015. The major and trace element glass compositions of the productive Mediterranean volcanic sources: tools for correlating distal tephra layers in and around Europe. Quat. Sci. Rev. 118, 48–66.
Unnikrishnan, A., Chhabra, R.P., 1991. An experimental study of motion of cylinders in Newtonian fluids: wall effects and drag coefficient. Can. J. Chem. Eng. 69 (3), 729–735.
Voth, G.A., Soldati, A., 2017. Anisotropic particles in turbulence. Annu. Rev. Fluid Mech. 49, 249–276.
Wadell, H., 1933. Sphericity and roundness of rock particles. J. Geol. 41 (3), 310–331.
Wastegård, S., 2002. Early to middle Holocene silicic tephra horizons from the Katla volcanic system, Iceland: new results from the Faroe Islands. J. Quat. Sci. 17 (8), 723–730.
Wastegård, S., Björck, S., Possnert, G., Wohlfarth, B., 1998. Evidence for the occurrence of Vedde Ash in Sweden: radiocarbon and calendar age estimates. J. Quat. Sci. 13 (3), 271–274.
Watson, E.J., Swindles, G.T., Stevenson, J.A., Savov, I., Lawson, I.T., 2016. The transport of Icelandic volcanic ash: Insights from northern European cryptotephra records. J. Geophys. Res. Solid Earth 121 (10), 7177–7192.
Webster, H.N., Thomson, D.J., 2011. Dry deposition modelling in a Lagrangian dispersion model. Int. J. Environ. Pollut. 47 (1–4), 1–9.
Webster, H.N., Thomson, D.J., 2014. The NAME wet deposition scheme. Met Office Forecasting Research Technical Report. Met Office, UK, p. 584.
Webster, H.N., Carroll, E.B., Jones, A.R., Manning, A.J., Thomson, D.J., 2007. The Buncefield oil depot incident: a discussion of the meteorology. Weather 62 (12), 325–330.
Webster, H.N., Thomson, D.J., Johnson, B.T., Heard, I.P.C., Turnbull, K., Marenco, F., Kristiansen, N., Dorsey, J., Minikin, A., Weinzierl, B., Schumann, U., Sparks, R.S.J., Loughlin, S.C., Hort, M.C., Leadbetter, S.J., Devenish, B.J., Manning, A.J., Witham, C.S., Haywood, J.M., Golding, B.W., 2012. Operational prediction of ash concentrations in the distal volcanic cloud from the 2010 Eyjafjallajökull eruption. J. Geophys. Res. Atmos. 117 (D20).
White, F.M., 1974. Viscous Fluid Flow. McGraw-Hill, New York.
Wilkins, K.L., Mackie, S., Watson, M., Webster, H.N., Thomson, D.J., Dacre, H.F., 2016. Data insertion in volcanic ash cloud forecasting. Ann. Geophys. 57.
Willmarth, W.W., Hawk, N.E., Harvey, R.L., 1964. Steady and unsteady motions and wakes of freely falling disks. Phys. Fluids 7 (2), 197–208.
Wilson, L., Huang, T.C., 1979. The influence of shape on the atmospheric settling velocity of volcanic ash particles. Earth Planet. Sci. Lett. 44 (2), 311–324.
Witham, C., Hort, M., Thomson, D., Leadbetter, S., Devenish, B., Webster, H., Beckett, F., Kristiansen, N., 2017. The current volcanic ash modelling setup at the London VAAC. UK Meteorological Office Technical Summary v1.4. Met Office, UK.